Draft version October 29, 2007
Preprint typeset using LaTeX style emulateapj v. 7/15/03

DELAYED NEUTRINO-DRIVEN SUPERNOVA EXPLOSIONS AIDED BY THE STANDING ACCRETION-SHOCK INSTABILITY

A. Marek[1] and H.-Th. Janka[1]

Draft version October 29, 2007

ABSTRACT

We present results of two-dimensional hydrodynamic simulations of stellar core collapse, which confirm that the neutrino-heating mechanism remains a viable explanation of the explosion of a wider mass range of supernova progenitors, but the explosion sets in later and develops differently than thought so far. The calculations were performed with an energy-dependent treatment of the neutrino transport based on the "ray-by-ray plus" approximation, in which the neutrino number, energy, and momentum equations are closed with a variable Eddington factor obtained by iteratively solving a model Boltzmann equation. We focus here on the evolution of a $15\,M_\odot$ progenitor and provide evidence that shock revival and most likely an explosion are initiated at about 600 ms after core bounce, powered by neutrino energy deposition. Similar to previous findings for an $11.2\,M_\odot$ star, but significantly later, the onset of the explosion is fostered by the standing accretion shock instability (SASI). This instability exhibits highest growth rates for the dipole and quadrupole modes, which lead to large-amplitude bipolar shock oscillations and push the shock to larger radii, thus increasing the time accreted matter is exposed to neutrino heating in the gain layer. As a consequence, also convective overturn behind the shock is strengthened, which otherwise is suppressed or damped because of the small shock stagnation radius. When the explosion sets in, the shock reveals a pronounced global deformation with a dominant dipolar component. A "soft" nuclear equation of state that causes a rapid contraction and a smaller radius of the forming neutron star and thus a fast release of gravitational binding energy, seems to be more favorable for the development of an explosion. Rotation has the opposite effect because it leads to a more extended and cooler neutron star and thus lower neutrino luminosities and mean energies and less neutrino heating. Neutron star g-mode oscillations and the acoustic mechanism play no important role in our simulations. While numerical tests show that our code is well able to follow core g-modes if they are instigated, the amplitude of such oscillations remains very small in the supernova runs and the acoustic energy flux injected by the ringing neutron star is minuscule compared to the neutrino energy deposition.

Subject headings: supernovae — hydrodynamics — neutrinos

1. INTRODUCTION

The physical processes that start the explosion of massive stars are still not well understood, although this is of crucial importance for predicting supernova and remnant properties, nucleosynthesis conditions and yields, and the observable signals from supernovae like neutrinos and gravitational waves. Neutrinos are thought to be the main agent of energy transport and energy loss from collapsing stars, an expectation that was spectacularly verified by the detection of two dozen neutrinos in connection with Supernova 1987A. Colgate & White (1966) suggested already 40 years ago that the intense flux of neutrinos radiated from the nascent neutron star might deposit the energy needed to reverse the stellar collapse. The detailed physics of this neutrino-driven mechanism, however, was worked out only later, based on numerical results of Wilson (1985). Bethe & Wilson (1985) showed that neutrinos deposit their energy behind the stalled supernova shock front mainly by the absorption of ν_e and $\bar{\nu}_e$ on free neutrons and protons, respectively, which are the most abundant nuclear species in the postshock layer. Provided the neutrino luminosities are sufficiently large, this energy input was found to be so strong that the stagnating shock can be "revived" and thus accelerates outward to propagate through the overlying, still collapsing layers of the star.

The viability of this neutrino-heating mechanism has recently been demonstrated for stars near the lower mass end of supernova progenitors for stiff as well as soft nuclear equations of state (Kitaura, Janka, & Hillebrandt 2006, Janka et al. 2007a). The investigated progenitor with a main-sequence mass of $8.8\,M_\odot$ (Nomoto 1984, 1987) can be considered as representative of the ~ 8–$10\,M_\odot$ range. The cores of such stars consist of oxygen, neon, and magnesium instead of iron and possess an extremely steep density gradient at their surface. The latter fact leads to a very rapid decrease of the mass accretion rate onto the forming neutron star, enabling the stalled shock to continue its expansion. This creates favorable conditions for neutrino energy deposition, thus allowing a neutrino-driven baryonic wind to be launched, which is sufficiently powerful to eject the gravitationally loosely bound outer layers of the star. The new results confirm qualitatively previous simulations by Mayle & Wilson (1988), although the more sophisticated treatment of the neutrino transport in the new models, which were computed with the Prometheus-Vertex code, leads to the predictions of a lower explosion energy and a lower neutron excess in the ejecta.

Electronic address: amarek@mpa-garching.mpg.de
Electronic address: thj@mpa-garching.mpg.de
[1] Max-Planck-Institut für Astrophysik, Karl-Schwarzschild-Str. 1, D-85741 Garching, Germany

In case of more massive progenitors, Wilson & Mayle (1988, 1993) could obtain explosions only by assuming that the neutrino luminosities and thus the neutrino energy deposition behind the stalled shock were boosted by enhanced neutrino transport in the neutron star. According to Wilson & Mayle this could happen, e.g., because of the presence of neutron-finger instabilities below the neutrinosphere. The existence of neutron-finger unstable conditions, however, was repudiated on grounds of a detailed analysis of the neutrino transport conditions in supernova cores (Bruenn & Dineva 1996). Nevertheless, numerical simulations (Buras et al. 2006b; see also Dessart et al. 2006) showed that Ledoux convection occurs inside the proto-neutron star and later than about 200 ms after bounce leads to accelerated lepton number and energy losses because of significantly increased muon and tau neutrino luminosities. The fluxes of ν_e and $\bar{\nu}_e$, which are mostly responsible for the shock heating, however, hardly change on a post-bounce timescale of some hundred milliseconds, and the mean energies of the radiated neutrinos and antineutrinos of all flavors even decrease compared to models that ignore convection.

A potentially stronger multi-dimensional effect that is clearly supportive for delayed shock revival, was discovered to be convective overturn in the layer behind the stagnant shock. In this region neutrino heating tends to create a negative entropy gradient, because the energy deposition is maximal just outside of the gain radius (Herant et al. 1994; Burrows, Hayes, & Fryxell 1995, Janka & Müller 1996). Cooler matter that is accreted by the shock is carried in narrow downdrafts closer to the gain radius, where it readily absorbs energy from the neutrinos. At the same time, heated matter with its higher entropy becomes buoyant and starts rising and expanding, thus reducing energy loss by the reemission of neutrinos and pushing the shock farther out. Convective overturn therefore improves the efficiency of the neutrino energy transfer because it allows more matter to be exposed to strong heating near the gain radius. Effectively this means that the mass in the gain layer grows and that gas stays there for a longer time. This is reflected by an increase of the mean timescale τ_{adv} needed by accreted matter to move inward from the shock to the gain radius. A larger value of τ_{adv} implies that the ratio of the advection timescale to the neutrino-heating timescale, τ_{heat}, gets closer to unity, which is a necessary condition for a model to approach an explosion (see the analysis in Buras et al. 2006b and also Thompson, Quataert, & Burrows 2005).

Convection in the flow between shock and gain layer, however, is subject to strong damping because the gas is falling rapidly and the time for seed perturbations to grow is therefore short until the gas crosses the gain radius and reaches the Ledoux-stable cooling region (Foglizzo, Scheck, & Janka 2006). Convective activity is therefore *not* able to develop in the gain layer despite the negative entropy gradient there, unless the initial density perturbations are sufficiently large or the ratio of advection timescale to convective growth timescale, τ_{conv}, exceeds a critical value (for more details, see Scheck et al. 2007). Two-dimensional (2D) supernova simulations (Buras et al. 2006a, 2006b) with the Prometheus-Vertex code, employing a sophisticated energy-dependent description of the neutrino transport, indeed show that convective overturn in the hot-bubble region becomes much less vigorous than in previous multi-dimensional models with a grey neutrino diffusion scheme (e.g., Herant et al. 1994; Burrows et al. 1995; Fryer 1999; Fryer & Warren 2002, 2004), mainly because the accretion shock in the new models lingers at rather small radii and the correspondingly high infall velocities in the postshock region are unfavorable for the growth of convection. Scheck et al. (2007), performing parametric hydrodynamic studies of the post-bounce accretion phase in collapsing stellar cores, found that convection is suppressed when (i) the neutrino heating is too weak to produce a steep entropy gradient behind the shock, or (ii) the rapid contraction of the nascent neutron star leads to shock retraction and thus causes very short infall timescales of the gas between shock and gain radius.

In such a situation, however, the standing accretion shock instability (SASI; Blondin, Mezzcappa, & DeMarino 2003), a generic hydrodynamic instability of the shocked accretion flow to non-radial deformation modes, can exhibit particularly large growth rates (cf. Scheck et al. 2007) and becomes the dominant multi-dimensional phenomenon to initiate shock expansion. This was seen in the studies by Scheck et al. (2007) and is confirmed by the linear stability analysis of Yamasaki & Yamada (2007). The SASI stimulates large-amplitude bipolar shock oscillations, which create strong entropy variations in the postshock flow and thus trigger violent secondary convection. This helps pushing the stalled shock to larger radii and therefore stretches the time accreted matter is exposed to neutrino heating in the gain layer, establishing healthy conditions for the success of the neutrino-driven mechanism.

Such a decisive role of the SASI was indeed observed in case of an $11.2\,M_{\odot}$ progenitor, whose collapse and explosion were simulated with the Prometheus-Vertex code (Buras et al. 2006b). Only when the setup of the numerical grid did not prohibit the growth of the lowest (dipolar and quadrupolar) SASI modes[2], which have the largest growth rates, could an explosion be obtained. Convection alone was too weak to yield sufficient support for the neutrino-heating mechanism. Instead it was the SASI in the first place which pushed the shock farther out and helped to bring the ratio of advection timescale to neutrino-heating timescale closer to the critical value of unity, which is necessary for reversing accretion to explosion.

In this paper we will present evidence that this SASI-aided neutrino-heating mechanism may initiate explosions for a wider mass range of progenitor stars. We investigate here a $15\,M_{\odot}$ model (s15s7b2 from Woosley & Weaver 1995) which is frequently used in previous and present core-collapse studies because it can be considered as representative of stars in a larger mass interval. Stellar evolution calculations by Woosley, Heger, & Weaver (2002), for example, produced a very similar core structure also for other supernova progenitors up to about $20\,M_{\odot}$ (see model s20.0 in Figs. A.2 and A.3 of Buras et al. 2006b). We discuss results of a 2D simulation in which

[2] In previous simulations with failed explosions (Buras et al. 2003a) the computational volume was constrained to a lateral wedge of 90 degrees ($\pm 45°$) around the equatorial plane, using periodic boundary conditions. This setup prevented the occurrence of the dipole and quadrupole SASI modes.

a modest amount of rotation was assumed and which develops an explosion at 600 ms after core bounce, and compare it with non-exploding spherically symmetric (1D) simulations on the one hand, and 2D models without rotation on the other, in which two different equations of state (EoSs) for supernova matter are used, namely the Lattimer & Swesty (1991) EoS with a soft nuclear phase and the Hillebrandt, Wolff, & Nomoto (1984; see also Hillebrandt & Wolff 1985) EoS with a significantly stiffer nuclear phase (Hillebrandt 1994). Both are consistent with current neutron star mass determinations but the former leads to significantly more compact proto-neutron stars than the latter. The rotating pre-collapse iron core has a spin period of about 12 seconds. This is roughly a factor of ten more rapid than predicted by recent stellar evolution models including magnetic fields (Heger, Woosley, & Spruit 2005), but considerably slower than necessary for magnetohydrodynamics to be important in triggering the explosion, which requires pre-collapse spin periods of 2–3 seconds (Burrows et al. 2007a, Thompson et al. 2005).

We have also evaluated our simulations for the presence of gravity waves in the nascent neutron star. Burrows et al. (2006, 2007b) found in their 2D supernova models that the anisotropic accretion flow (as a consequence of the SASI) excited the neutron star to vigorous g-mode oscillations, in particular also the dipole ($l = 1$) mode. The amplitude of these oscillations became so large (about 3 km) at the neutron star surface that a sizable acoustic energy flux was driven into the surrounding gas and was transporting a significant amount of acoustic energy to the stalled supernova shock. Burrows et al. did not find any neutrino-driven explosions in their models. However, at late times (typically at $t > 1$ s after bounce), and therefore much later than the shock is revived by the neutrino-heating mechanism in the $11.2\,M_\odot$ simulation of Buras et al. (2006b) and in the $15\,M_\odot$ model discussed here, the acoustic energy flux caused by the core g-mode oscillations became dominant compared to neutrino heating and was able to cause an explosion. In our simulations the g-mode oscillations of the newly formed neutron star have amplitudes that are always smaller by roughly a factor of 100 compared to those in the models of Burrows et al. (2006, 2007b) at the time when acoustically driven explosions were obtained. In order to make sure that our neutrino-hydrodynamics code is able to deal with this potentially important physical effect, we have also performed numerical tests. These demonstrate that our code is well able to track large-amplitude g-modes, also of dipole character, if such modes are excited in the neutron star core.

The reason why Burrows et al. (2006, 2007b) did not see any neutrino-driven explosions, which is in contrast to our findings, is not clear. However, the numerical approaches of both groups and the included physics differ in many aspects. While our "ray-by-ray plus" treatment of neutrino transport is highly sophisticated in dealing with the energy dependence of the problem but describes its dependence on the polar angle only approximately, Burrows et al. applied a 2D neutrino diffusion scheme, in which the energy dependence was only incompletely taken into account, because energy-bin coupling was ignored and Doppler effects due to the motion of the stellar fluid were neglected. In addition, the Tucson group made use of a different numerical method to solve the hydrodynamics equations, e.g. the gravitational force was implemented in the momentum equation in an uncommon, momentum-conserving way. In their VULCAN code they employed a polar grid only in the outer regions of the computational volume but cartesian coordinates in the central part. They did their simulations with the nuclear EoS of Shen et al. (1998), which is significantly stiffer than the Lattimer & Swesty EoS though fairly similar to the Hillebrandt & Wolff EoS (Marek et al., in preparation; see also Janka et al. 2007b), and their models were computed with purely Newtonian gravity, whereas a significantly stronger relativistic gravitational potential according to Marek et al. (2006) is applied in our models.

Our paper is structured as follows: In Sect. 2.1 we give a brief summary of the numerical scheme and physics input used in the presented simulations, an overview of which follows in Sect. 2.2. Section 3 contains our results. For reference, we present in Sect. 3.1 results of our 1D simulations for the two employed nuclear EoSs, then describe the dynamical evolution of our exploding model in Sect. 3.2, compare the different computational runs in Sect. 3.3, and discuss our neutrino results in Sect. 3.4. An analysis of neutron star g-modes including numerical tests is presented in Sect. 4. In Sect. 5 we summarize our findings and draw conclusions.

2. METHODS AND MODELS

In this section we briefly summarize the basic properties of our numerical code and the input physics used in this work. We then give a compilation of the core-collapse simulations whose results are described afterwards.

2.1. *Numerical approach and input physics*

The core-collapse and post-bounce calculations presented in this work were performed with the PROMETHEUS-VERTEX neutrino-hydrodynamics code, details of which were published by Rampp & Janka (2002) and Buras et al (2006a). The code module that integrates the nonrelativistic hydrodynamics equations is a conservative and explicit Eulerian implementation of a Godunov-type scheme with higher-order spatial and temporal accuracy. The self-gravity of the stellar gas is treated in an approximation to general relativity, in which the monopole term of the Newtonian potential is replaced by an effective relativistic scalar potential that was constructed from close comparison of the Newtonian and relativistic equations of motion (for details, see Marek et al. 2006). For this effective relativistic monopole potential we consider the Cases A and R of the Marek et al. paper. The higher-order terms of the gravitational potential are taken as solutions of the Poisson equation for the two-dimensional gas distribution (see Müller & Steinmetz 1995).

The time-implicit transport routine solves the moment equations of neutrino number, energy, and momentum in spherical symmetry, employing a variable Eddington factor for closing the set of equations (Rampp & Janka 2002). The closure factor is obtained from a simplified Boltzmann equation, whose integro-differential character is tackled by iterating the coupled system of Boltzmann and moment equations until convergence is achieved.

Our treatment of the neutrino transport and of neutrino-matter interactions is energy dependent and includes the full redistribution of neutrinos in energy and momentum space by scattering reactions with electrons, positrons, and nucleons. Effects caused by the motion of the stellar fluid are taken into account as well as general relativistic redshifting and time dilation. In two spatial dimensions the transport is based on the "ray-by-ray plus" approximation, in which spherically symmetric transport problems are solved for the conditions present in the radial "rays" corresponding to the different lateral bins of the polar grid. This means that we assume the local neutrino phase-space distribution to be axially symmetric around the radial direction and thus to depend only on one instead of two angles, as a consequence of which the neutrino pressure tensor remains diagonal and the lateral component of the neutrino flux vanishes. This simplifies the transport from a five dimensional, time-dependent problem (with variables being the radius, energy, polar angle, and two angles that characterize the neutrino momentum direction) to only four dimensions and reduces the complexity of the moment equations significantly (see Appendix B in Buras et al. 2006a) at the expense of neutrino shear and non-radial flux of the neutrinos, which are disregarded in such an approach. However, the moment equations still contain the terms that account for the advection of trapped neutrinos with the stellar fluid motion in the lateral direction. Moreover, the lateral component of the neutrino pressure gradient is included in the hydrodynamics equations.

Comparison of our approximative treatment of general relativity with fully relativistic simulations revealed excellent agreement in spherical symmetry and still good agreement in two dimensions when the rotation did not become too extreme (see Marek et al. 2006, Liebendörfer et al. 2005).

A state-of-the-art treatment of the interactions of neutrinos (ν) and antineutrinos ($\bar{\nu}$) of all flavors (Buras et al 2006a, Marek et al. 2005) is applied in our simulations, including all relevant β-processes, thermal processes, and the scattering off electrons, positrons, nucleons, and nuclei. In neutral-current and charged-current neutrino-nucleon reactions the effects of nucleon recoil and thermal motions as well as nucleon correlations in the dense medium are taken into account (see Buras et al. 2006a, and references therein). Neutrino-nucleon scattering just like neutrino-electron scattering is therefore a channel for energy exchange between neutrinos and the stellar medium and fosters neutrino thermalization, thus leading to a noticeable reduction of the mean energy and a spectral pinching of radiated neutrinos, in particular of muon and tau flavor (Keil, Raffelt, & Janka 2003). Electron captures on heavy nuclei are described by making use of the improved data of Langanke et al. (2003), who constructed a table for the capture rates of a large ensemble of nuclei in nuclear statistical equilibrium. Also interactions of neutrinos of different flavors, scatterings as well as neutrino-antineutrino pair conversion (Buras et al. 2003b) are included in our treatment.

We employ two different nuclear equations of state (EoSs) in our simulations. On the one hand, we use a soft version of the compressible liquid drop EoS of Lattimer & Swesty (1991; see also Lattimer et al. 1985; "LS-EoS") with an incompressibility modulus of bulk nuclear matter of 180 MeV and a symmetry energy parameter of 29.3 MeV. On the other hand we perform simulations with the considerably stiffer EoS of Hillebrandt & Wolff (1985, see also Hillebrandt et al. 1984; "HW-EoS"), which is based on a Hartree-Fock calculation, assuming a Skyrme force for the nucleon-nucleon interaction with parameters given by Köhler (1975). Its incompressibility has a value of 263 MeV and the symmetry energy was chosen to be 32.9 MeV. Details of the calculation can be found in Hillebrandt et al. (1984) and Hillebrandt & Wolff (1985). Both EoSs yield different maximum masses of stable, nonrotating neutron stars. In case of the LS-EoS the maximum gravitational mass is $1.84\,M_\odot$, whereas it is $2.21\,M_\odot$ for the HW-EoS, which are both compatible with measured neutron star masses (Lattimer & Prakash 2007). Both EoSs also lead to a significantly different evolution of the radius of the nascent neutron star as a function time (see Fig. 7 in Janka et al. 2007b). While the LS-EoS produces rather compact neutron stars with a radius of $R_{\rm ns} = 11.9$ km for a cold star with $1.4\,M_\odot$ and $R_{\rm ns} = 10.0$ km for a cold star near the maximum mass, the corresponding radii are 13.94 km and 13.5 km for the HW-EoS (cf. Marek 2007).

We apply the nuclear EoS (either LS or HW) only above a transition density $\rho_{\rm EoS}$. In the low-density regime, $\rho < \rho_{\rm EoS}$, the EoS includes the ideal gas contributions of electrons and positrons (of arbitrary degrees of relativity and degeneracy), photons, and a mixture of non-relativistic classical Boltzmann gases of neutrons, protons, α particles, and 14 kinds of heavy nuclei. Coulomb lattice corrections of the pressure, energy density, entropy, and adiabatic index are taken into account. Above a temperature of $T_{\rm NSE} = 0.5$ MeV the nuclear constituents are assumed to obey nuclear statistical equilibrium (NSE), whereas below this temperature only nuclear burning of silicon and oxygen (and similarly neon and magnesium), and carbon (implemented according to the "flashing" treatment by Rampp & Janka 2002, Appendix B.2) can change the composition. The value of $\rho_{\rm EoS}$ is chosen such that a smooth transition of pressure, internal energy density, and chemical potentials as functions of density is guaranteed. During the collapse phase $\rho_{\rm EoS}$ is set to $6 \times 10^7\,{\rm g\,cm^{-3}}$ in case of the LS-EoS and $1.5 \times 10^9\,{\rm g\,cm^{-3}}$ for the HW-EoS, while after core bounce, when α particles can reach a significant mass fraction and an error in the LS-EoS (Fryer, private com-

Table 1. Investigated $15\,M_\odot$ models.

Model	Dimension	N_r [a]	N_θ [b]	N_ϵ [c]	$\Phi_{\rm eff}$ [d]
M15LS-1D	1D	600–960	1	17	new
M15HW-1D	1D	600–750	1	17	new
M15LS-rot	2D & rotation	400–850	128	17	old
M15LS-2D	2D	600–960	192	17	new
M15HW-2D	2D	600–700	192	17	new
M15LS-rot9	2D & rotation	400–500	128	9	new

[a] Number of radial grid points, increasing with time.
[b] Number of lateral grid points from pole to pole.
[c] Number of energy grid points for the neutrino transport.
[d] Effective relativistic potential; "old" corresponds to definition introduced by Rampp & Janka (2002), which is equivalent to Case R of Marek et al. (2006); "new" corresponds to Case A of Marek et al. (2006).

munication) is potentially relevant (see, however, Buras et al. 2006a), we use $\rho_{\rm EoS} = 10^{11}\,{\rm g\,cm^{-3}}$.

2.2. *Investigated models*

The core-collapse and supernova runs computed for this work are listed in Table 1. All of them are based on the $15\,M_\odot$ progenitor s15s7b2 from Woosley & Weaver (1995). Two of the calculations are performed in spherical symmetry, one with the LS-EoS (indicated by "LS-1D" in the model name) and another one with the HW-EoS (labeled by "HW-1D"). These are compared with four 2D (axially symmetric) simulations, two of which (M15LS-2D and M15HW-2D) are computed without rotation, using the EoSs also employed in the 1D models. In the other two simulations (i.e., our reference long-time run, M15LS-rot, and Model M15LS-rot9) we impose rotation on the progenitor core with initially a constant angular frequency of $0.5\,{\rm rad\,s^{-1}}$ (corresponding to a rotation period of about 12 s) inside the Fe core and an $r^{-3/2}$ decline outside (see Fig. 1 in Müller et al. 2004 and Sect. 3.4 in Buras et al. 2006b). This rotation rate is roughly a factor ten faster than current predictions for pre-collapse stellar cores by Heger et al. (2005), but too slow for the free energy reservoir in the secularly evolving proto-neutron star to be sufficient to power magnetohydrodynamic explosions (see Burrows et al. 2007a and Thompson et al. 2005).

In all of our nonrotating models we have implemented for the monopole of the gravitational potential the effective relativistic potential according to Case A of Marek et al. (2006), which in that paper was identified to yield the best results in comparison to spherically symmetric, fully relativistic simulations. For models with core rotation, however, the best choice of the effective gravitational potential is less obvious. While for slow rotation Case A still produces the most satisfactory results, this monopole term is not able to account for the relativistic gravity of rotationally deformed cores. In such a situation, Marek et al. (2006) found Case R to be the better representation, because, e.g., it leads to central densities closer to those of the relativistic calculation. Several 100 ms after core bounce even our slowly rotating pre-collapse model develops a sizable oblate deformation of the nascent neutron star. Since late-time effects are the main interest of our present investigations, we therefore decided to employ the effective relativistic TOV potential of Case R of Marek et al. (2006) in our reference long-time 2D simulation (Model M15LS-rot) and to compare this model with another simulation that includes rotation and uses Case A for the monopole term of the gravitational potential (Model M15LS-rot9).

Our models are computed with 400–1000 non-equidistant radial zones, which are chosen such that the resolution $\Delta r/r$ is typically better than three percent in the interior of the neutron star and between less than one percent and 1.5 percent around the neutrinospheres and outside of the neutron star. During the simulations the number of radial grid zones N_r is increased (Table 1 gives N_r at the beginning and at the end of the different runs) and the region of higher resolution is moved to smaller radii in order to follow the contraction of the neutron star and to ensure good resolution at the neutron star surface where the density gradient steepens with time. We make sure that at least 20 radial zones are used per density decade, corresponding to at most 12% density variation between neighboring zones. The representation of hydrostatic equilibrium as well as the accurate computation of the neutrino transport in the decoupling layer require at least this numerical resolution; in case of the transport the luminosity variation from zone to zone is a limiting factor. Convergence tests for our code showed that insufficient radial resolution in particular in this region may not only lead to bloated surface layers of the neutron star and to an overestimation of the neutrino luminosities, but as a consequence also to artificial explosions even of spherically symmetric models. In order to make sure that our exploding 2D simulation, Model M15LS-rot, is well resolved, we recomputed a significant part of the crucial evolution phase of this model with about half the radial zone width in the neutron star surface layer. This high-resolution run, Model M15LS-rot-hr, is not listed in Table 1, but some of the plots will also show results from this calculation for comparison.

Our 2D simulations are performed with 128 or 192 equidistant lateral zones from pole to pole of the spherical coordinate grid (Table 1). Comparing results for both resolutions we found excellent quantitative agreement of the neutron star and neutrino properties (which implies that the lateral resolution is sufficient for describing neutron star convection) and very good qualitative agreement of the shock evolution (because of the chaotic character of hydrodynamic instabilities in the hot-bubble region, a detailed quantitative agreement cannot be expected). At the grid center, however, a small region (1.7 km in radius or six radial zones) is computed in spherical symmetry to avoid the most severe limitation of the hydrodynamics timestep due to the Courant-Friedrich-Lewy condition.

In the transport module of our code we usually employ 17 geometrically distributed energy bins for neutrinos between 0 and 380 MeV. One of our models, M15LS-rot9, is computed only with nine energy bins, which leads to a reduced steepness of the high-energy tail of the neutrino spectrum roughly three orders of magnitude and more below the spectral peak. Spherically symmetric test calculations, however, show that this lower accuracy of the neutrino transport has hardly any influence on the hydrodynamic evolution of the supernova core and also causes only small differences (of order 10%) in the luminosities and mean energies of the radiated neutrinos. Using nine instead of 17 energy bins reduces the CPU time requirements of a simulation by nearly a factor of seven.

The 2D runs without rotation are started at core bounce after mapping the corresponding 1D models to the 2D grid and imposing random zone-to-zone variations of the radial velocity component (or density) with an amplitude of one percent. The rotating models are computed in 2D from the onset of the collapse with random perturbations and the initial rotation law imposed on the spherically symmetric progenitor star (for details, see Buras et al. 2006b).

Running 2D models with a sophisticated energy-dependent treatment of the neutrino transport for many hundred milliseconds after bounce poses a considerable numerical challenge, because the rapid variations of the accretion flow in the presence of violent hydrodynamic instabilities in the postshock region do not allow the (im-

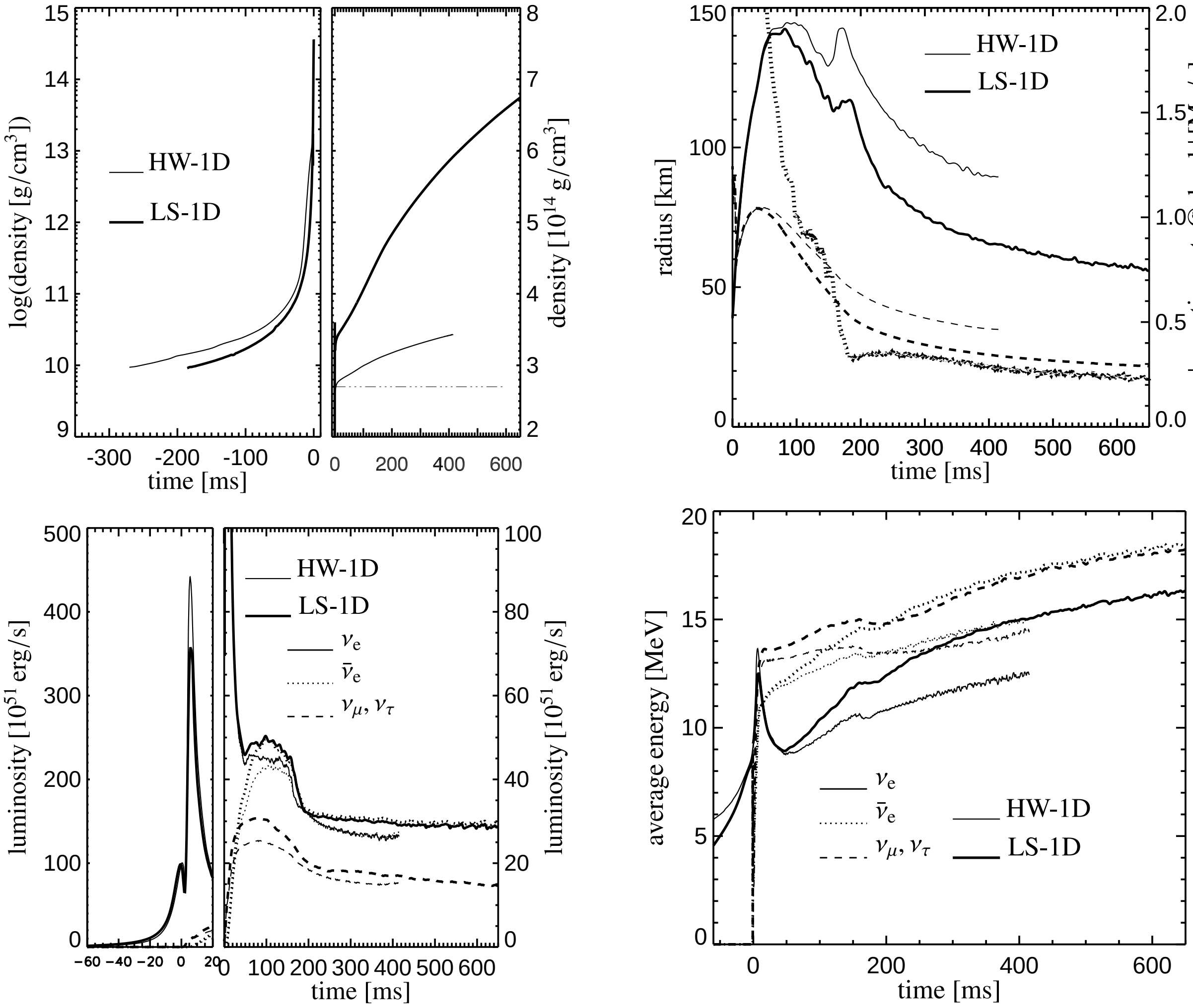

FIG. 1.— Results of our two 1D models, M15LS-1D (bold lines) and M15HW-1D. Time is normalized to the moment of core bounce. *Top left:* Central densities as functions of time. The horizontal dash-triple-dotted line marks the value of the nuclear saturation density, $\rho_0 \approx 2.7 \times 10^{14}\,\mathrm{g\,cm^{-3}}$. *Top right:* Radii of shock (solid lines) and electron neutrinosphere (dashed lines) as functions of time. The transient shock expansion around 170 ms after bounce is caused by a composition interface with sudden decrease of the mass accretion rate arriving at the shock. The mass accretion rate is displayed by the bold dotted line. *Bottom left:* Luminosities of electron neutrinos, electron antineutrinos, and muon or tau neutrinos (or their antiparticles) as functions of time. *Bottom right:* Mean energies of radiated neutrinos (computed as the ratio of energy to number flux) for electron neutrinos, electron antineutrinos, and heavy-lepton neutrinos and antineutrinos. The luminosities and mean energies are shown as measured by an observer at rest relative to the stellar center at 400 km (from where the gravitational redshift to infinity is negligibly small). The softer LS-EoS leads to a much larger central density, a significantly more compact neutron star and therefore considerably higher luminosities and mean energies of the radiated neutrinos.

plicit) neutrino transport timestep to become larger than about 2×10^{-6} s and therefore about 500.000 timesteps and 3×10^{18} floating point operations were needed for our most advanced 2D model MS15LS-rot, which was evolved to more than 600 ms after bounce. For this reason, CPU-time limitations did not permit us to follow all of our 2D models to such very late post-bounce times. Although the set of calculations of Table 1 is not finished in this sense (and currently we have no way to do that in an acceptable time frame), it nevertheless allows for some interesting conclusions concerning the possibility of getting neutrino-driven explosions late after bounce and the dependence of this result on the properties and the neutrino emission of the forming neutron star.

3. RESULTS

In this section we discuss our simulations, starting with the 1D results for reference, then continuing with the exploding long-time 2D simulation, and finally turning to the other 2D models, which allow us by comparisons to better understand the factors that are decisive for the explosion in the successful run.

3.1. *Spherically symmetric simulations*

In Fig. 1 the results of our two 1D simulations are shown in overview. The collapse of the stellar core until bounce is somewhat faster with the softer (i.e. here: its adiabatic index in the subnuclear regime is lower) LS-EoS, and the maximum density reached at bounce is $3.6 \times 10^{14}\,\mathrm{g\,cm^{-3}}$ compared to $3.0 \times 10^{14}\,\mathrm{g\,cm^{-3}}$ in case of the HW-EoS. The central density is measured at a distance of 1.65 km (i.e. in the sixth radial grid zone) where numerical fluctuations caused by the inner

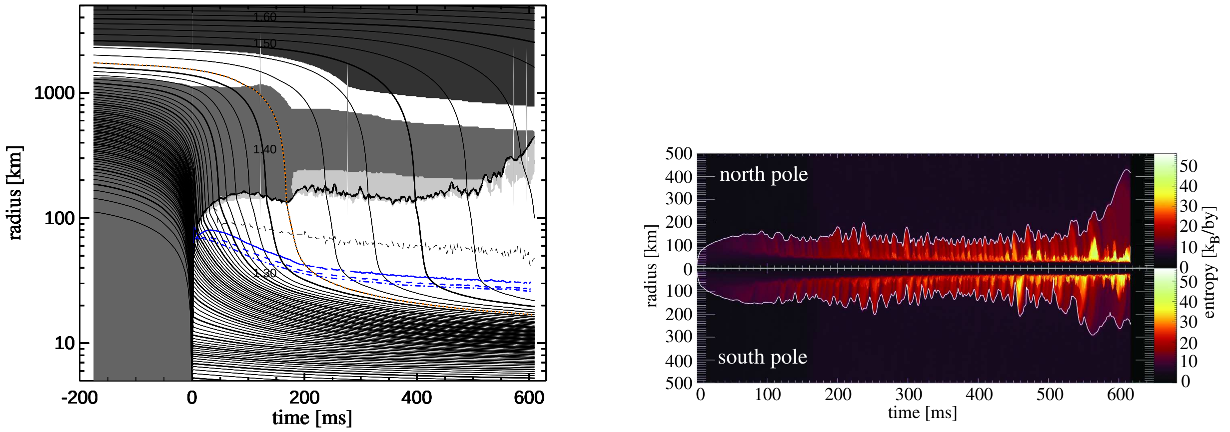

FIG. 2.— Evolution of Model M15LS-rot. *Left:* Mass shells versus time. In this 2D simulation with rotation, the mass-shell lines mark the radii that enclose certain values of the rest mass. The bold solid line indicates the (arithmetically) averaged shock position, the blue lines represent the mean neutrinospheres of ν_e (solid), $\bar{\nu}_e$ (dashed), and heavy-lepton neutrinos (dash-dotted), the black dashed curve indicates the mean gain radius, and the composition boundary between silicon shell and oxygen-enriched Si-layer at $1.42\,M_\odot$ is highlighted by a red dashed line. Dark grey denotes regions where the mass fraction of oxygen is larger than 10%, medium grey where the mass fraction of heavy nuclei with mass numbers $A \geq 56$ exceeds 10%, and light grey those regions where more than 30% of the mass is in α-particles. *Right:* Radial positions of the shock near the north and south poles as functions of post-bounce time (white lines). The color coding represents the entropy per nucleon of the stellar gas. The quasi-periodic, bi-polar shock expansion and contraction due to the SASI can be clearly seen.

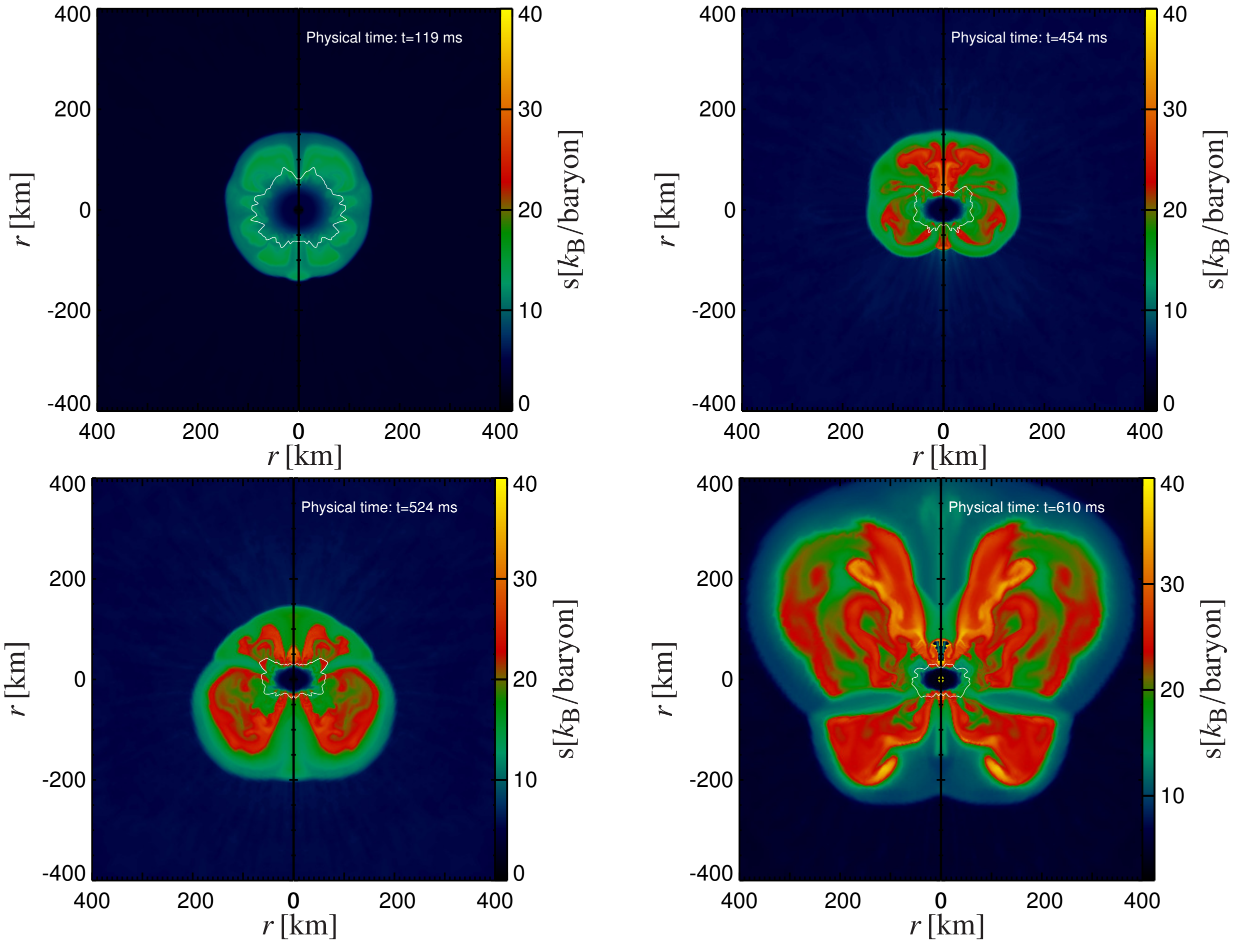

FIG. 3.— Four snapshots from the post-bounce evolution of Model M15LS-rot. The color coding represents the entropy of the stellar gas. The shock is visible as deformed sharp discontinuity between low-entropy, infalling matter in the upstream region and high-entropy, boiling matter behind the shock. The upper left plot shows the entropy distribution at $t = 119\,$ms after bounce, about 40 ms after the postshock convection has reached the nonlinear regime. The upper right and lower left plots ($t = 454\,$ms and $t = 524\,$ms after bounce) demonstrate the presence of a very strong bipolar oscillation due to the SASI, and the lower right plot ($t = 610\,$ms p.b.) displays the onset of a rapid outward expansion, most likely leading to an explosion, of the largely aspherical shock with a dominant $l = 1$ deformation mode. Note that the contracting nascent neutron star exhibits a growing prolate deformation because of the rotation considered in this simulation. The thin white line marks the direction-dependent location of the gain radius.

grid boundary are absent). During the post-bounce evolution the higher stiffness of the nuclear phase in the HW-EoS leads to a considerably lower central density and a clearly less rapid contraction of the nascent neutron star, visible from the larger radius of the electron neutrinosphere in the right upper panel of Fig. 1. Since the postshock layer is nearly in hydrostatic equilibrium during the quasi-stationary accretion phase of the stalled shock, the shock position $R_{\rm s}$ is a sensitive function of the neutron star radius, $R_{\rm ns}$, roughly as

$$R_{\rm s} \propto \left(\frac{R_{\rm ns}^4 T_{\rm ns}^4}{|\dot{M}|\, M_{\rm ns}^{1/2}}\right)^{2/3} , \qquad (1)$$

which follows from Eqs. (39), (56), and (63) of Janka (1991). Here $M_{\rm ns}$ is the neutron star mass, $T_{\rm ns}$ the temperature at the neutrinosphere, and $\dot{M}$ (<0) the rate of mass accretion by the shock. In case of the HW-EoS, the stagnation radius of the shock is therefore significantly larger during the phase of shock retraction ($t \gtrsim 80$–100 ms after bounce).

In contrast, the luminosities L_ν and mean energies $\langle\epsilon_\nu\rangle$ of the neutrinos radiated during shock accretion are appreciably higher in case of the LS-EoS, because the larger neutrinospheric temperature of the more compact neutron star overcompensates for the smaller radius (roughly, the ν_e emission behaves like blackbody radiation and thus $L_\nu \propto R_{\rm ns}^2 T_{\rm ns}^4$ and $\langle\epsilon_\nu\rangle \propto T_{\rm ns}$). Interestingly, the prompt ν_e burst during shock breakout reveals the opposite dependence on the nuclear EoS: it is more luminous in case of the HW-EoS because of a stronger deleptonization in a wider spatial region, which is facilitated by a less steep increase of the optical depth in the deleptonization region and thus an easier escape of the electron neutrinos.

We also point out that in the simulations with both EoSs the average energy of the radiated $\bar\nu_e$ gets very close to that of the emitted muon and tau neutrinos or becomes even slightly higher after about 200 ms of post-bounce accretion (Fig. 1, bottom right). This effect is visible in the mean spectral energies, which are defined as ratio of the energy flux to the number flux of neutrinos, $\langle\epsilon_\nu\rangle = \int_0^\infty {\rm d}\epsilon\, J_\nu(\epsilon)/\int_0^\infty {\rm d}\epsilon\,\epsilon^{-1}J_\nu(\epsilon)$, with $J_\nu(\epsilon)$ being the zeroth energy moment of the specific intensity. In contrast, the rms energies of the energy spectrum, $\langle\epsilon_\nu\rangle_{\rm rms} \equiv \left[\int_0^\infty {\rm d}\epsilon\,\epsilon^2 J_\nu(\epsilon)/\int_0^\infty {\rm d}\epsilon\, J_\nu(\epsilon)\right]^{1/2}$, still follow the standard order sequence, $\langle\epsilon_{\nu_e}\rangle_{\rm rms} < \langle\epsilon_{\bar\nu_e}\rangle_{\rm rms} < \langle\epsilon_{\nu_x}\rangle_{\rm rms}$, although the difference between the last two is considerably smaller than in older simulations, in which the transport treatment of heavy-lepton neutrinos ν_x did not take into account the energy exchange through neutrino-nucleon scatterings and the production of $\nu_x\bar\nu_x$ pairs by nucleon-nucleon bremsstrahlung and by the annihilation of $\nu_e\bar\nu_e$ pairs (for more details, see Buras et al. 2003b, Raffelt 2001, Keil et al. 2003). We will come back to a closer discussion of these interesting spectral properties in Sect. 3.4.

3.2. *Two-dimensional model with explosion*

In contrast to the spherically symmetric simulations, the two-dimensional Model M15LS-rot turns out to approach an explosive runaway situation after more than 500 ms of post-bounce accretion (Fig. 2). Some snapshots of the entropy distribution in the innermost 800 km for characteristic stages of the evolution are displayed in Fig. 3.

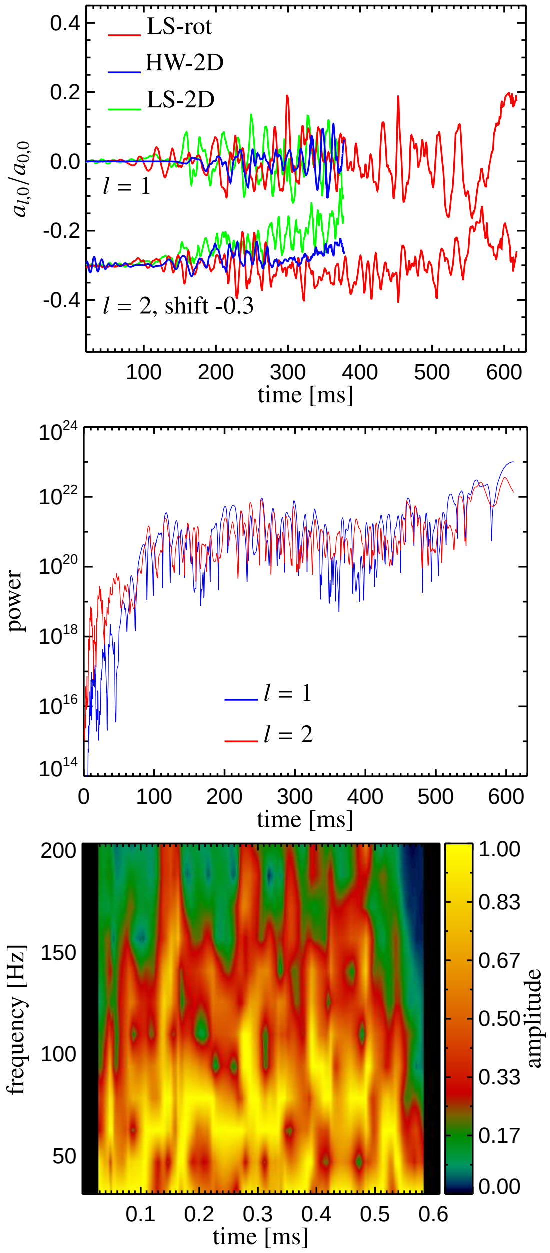

FIG. 4.— SASI and convective activity in Model M15LS-rot versus post-bounce time. *Top:* Coefficients of the dipole ($l = 1$) and quadrupole ($l = 2$) modes of the spherical harmonics expansion of the angle-dependent shock position, normalized to the amplitude of the $l = 0$ mode. For better visibility the curve of the $l = 2$ mode is shifted downward by 0.3 units. The results for Models M15LS-2D and M15HW-2D are also shown for comparison. *Middle:* Power of the $l = 1$ and $l = 2$ modes of the spherical harmonics expansion of the fractional pressure variations $[P(r,\theta) - \langle P(r,\theta)\rangle_\theta]/\langle P\rangle_\theta$, integrated over the volume between average electron neutrinosphere and average shock radius. *Bottom:* Frequency spectrum versus time of the power in $l = 1$ and $l = 2$ modes shown in the middle panel. The fourier analysis was performed every two milliseconds, sampling information in time windows of 64 ms width (which leads to discrete frequencies of 15.6 Hz and multiples), and the spectra were normalized on each time slice.

3.2.1. *Post-bounce evolution*

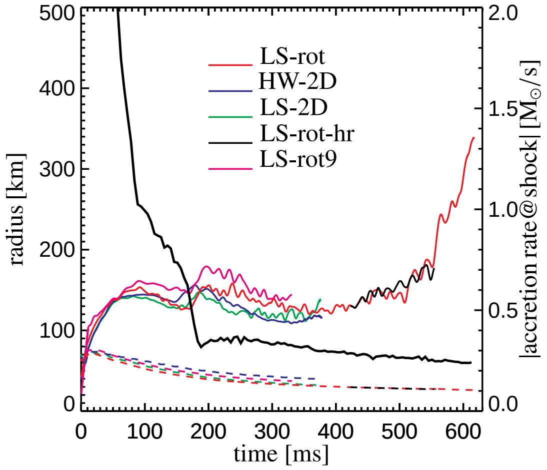

FIG. 5.— Average shock radii (solid) and average neutron star radii (dashed) for the set of computed 2D models as functions of post-bounce time (left vertical scale of the figure). The mean radius of the (in case of rotation deformed) neutron star is defined as arithmetic mean of all radial positions where the density equals $10^{11}\,\mathrm{g\,cm^{-3}}$. The bold black curve shows the time-dependent mass accretion rate just ahead of the shock in Model M15LS-rot (scale on the right vertical axis of the plot). The additional black line between 400 and about 550 ms corresponds to Model M15LS-rot-hr, which is a test calculation of Model M15LS-rot with significantly increased radial resolution in the neutron star surface and neutrino-heating layer.

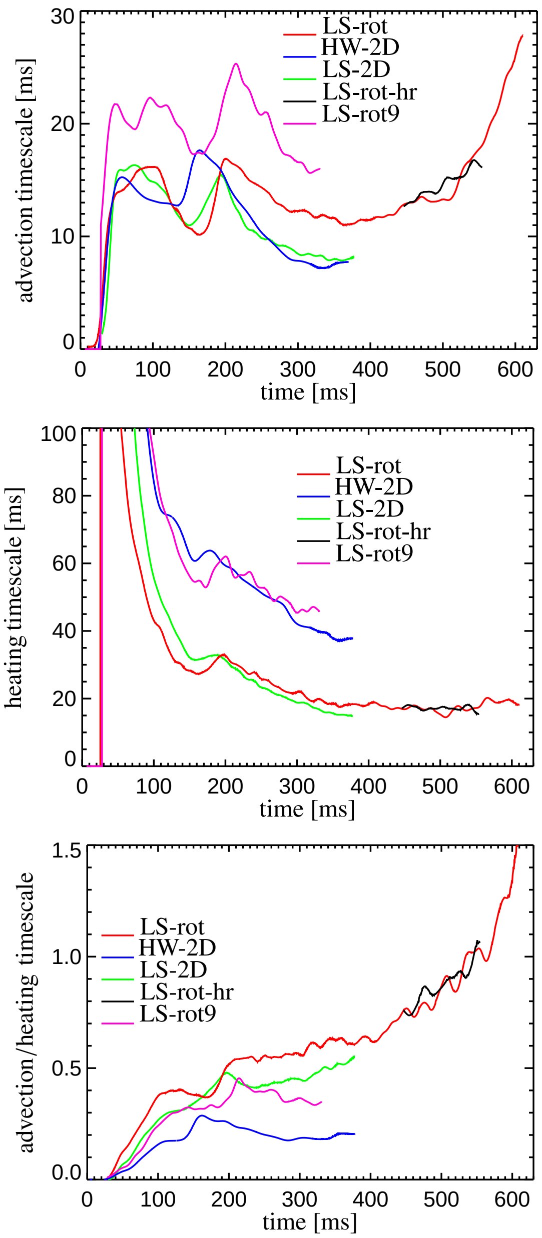

FIG. 6.— Dynamically important timescales for the set of computed 2D models as functions of post-bounce time. *Top:* Mean timescale for advection of accreted matter from the shock to the gain radius. *Middle:* Neutrino-heating timescale of matter in the gain layer. *Bottom:* Ratio of advection to heating timescale. The additional black line between 400 and about 550 ms corresponds to Model M15LS-rot-hr, which is a test calculation of Model M15LS-rot with significantly increased radial resolution in the neutron star surface and neutrino-heating layer.

The results of a 90-degree equivalent of this model (computed with a pole-to-equator wedge of the spherical coordinate grid and with reflecting conditions at both boundaries) until 300 ms after bounce were described by Buras et al. (2006b), see Sect. 3.4 there. Postshock convection is triggered by the small-scale perturbations that evolve from a 1% random initial (pre-collapse) seed during infall. It exhibits most rapid growth of high angular modes and creates visible inhomogeneities at 50–60 ms after bounce. In the 180-degree calculation discussed here, the first obvious differences between both hemispheres appear at about 100 ms and only shortly later (at $\sim$120 ms, see also the upper left snapshot in Fig. 3) low-amplitude bipolar shock oscillations set in, manifesting the development of a global, low-mode asymmetry. This can be seen in the top panel of Fig. 4, where large amplitudes of the dipolar ($l = 1$) and quadrupolar ($l = 2$) terms of a spherical harmonics expansion of the shock radius as a function of the polar angle θ show up at $t \gtrsim 100$ ms post bounce. The plot suggests that the dipole mode gains strength slightly faster and reaches large amplitudes some ten milliseconds earlier than the quadrupole mode.

The appearance of strong low-mode, quasi-periodic shock deformation is associated with sloshing motions of the whole accretion layer between shock and neutron star. The process is very similar to the phenomenon identified as SASI in the idealized accretion setup studied by Blondin et al. (2003) and seen also in more sophisticated post-bounce accretion simulations by Scheck et al. (2007). In those calculations convective activity was initially absent and set in only later, and therefore the oscillatory growth of the SASI in the linear regime could be clearly identified. In contrast, in the model discussed here, sufficiently strong neutrino heating and sufficiently large seed perturbations cause convective activity in the gain layer to develop readily on a short timescale after bounce. The early presence of convection masks the characteristic growth behavior of the SASI. We suspect that the acoustic waves and vorticity created by convection even accelerate the evolution of the SASI and the conditions for a linear description never exactly apply. The radii of the shock near the north pole and south pole in the right panel of Fig. 2 reveal

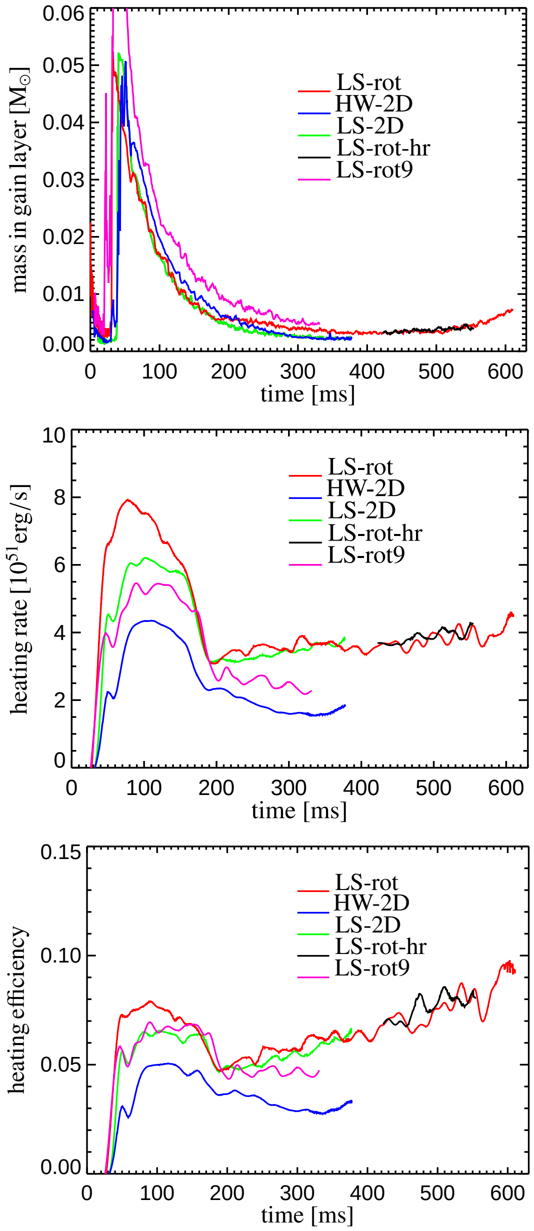

FIG. 7.— Neutrino heating conditions in the gain layer for the set of computed 2D models. Mass (*top*), total net rate of neutrino heating (*middle*), and neutrino heating efficiency (*bottom*) as functions of post-bounce time. The heating efficiency is defined as the ratio of the total heating rate to the sum of ν_e and $\bar{\nu}_e$ luminosities as seen in the observer frame. The additional black line between 400 and about 550 ms corresponds to Model M15LS-rot-hr, which is a test calculation of Model M15LS-rot with significantly increased radial resolution in the neutron star surface and neutrino-heating layer.

the alternating phases of shock expansion in the northern and southern hemispheres. The snapshots in Fig. 3 at 454 ms and 524 ms after bounce capture two such moments in which the shock inflates in opposite directions. The typical period of these SASI oscillations depends on the mean shock radius. It is about 10–12 ms when the shock is near 150 km (around 300–400 ms after bounce) and more like 15–17 ms when the average shock radius reaches 180–200 km, corresponding to power maxima at typical frequencies beween 50 Hz and 100 Hz. This can be seen in the time-dependent frequency spectrum of the low-mode SASI power (obtained from a fourier analysis of the quantity given in Eq. (2)) in the bottom panel of Fig. 4. The power spectrum has a very broad peak in the mentioned frequency interval and decays steeply towards higher frequencies.

The middle panel of Fig. 4 displays the corresponding total power of the $l = 1$ and $l = 2$ modes, computed as the volume integral of the squared dipole and quadrupole amplitudes of the fractional pressure variations between average neutrinosphere radius R_ν and average shock radius R_s,

$$\mathrm{Power}(l) \equiv 2\pi \int_{R_\nu}^{R_\mathrm{s}} \mathrm{d}r\, r^2\, a_l^2(r,t) \ , \qquad (2)$$

where $a_l(r,t)$ are the amplitudes of a spherical harmonics expansion of $[P(r,\theta,t) - \langle P(r,\theta,t)\rangle_\theta]/\langle P(r,\theta,t)\rangle_\theta$. The combined power of the two lowest modes turns out to reflect rather sensitively the dynamical activity in the accretion layer. One should note that during phases of relative quiescence of the dipole mode the quadrupole mode is dominant and vice versa. A high level of activity is reached shortly after convection has become strong and the SASI deformation of the shock has set in ($t \gtrsim$ 100 ms after bounce). The following slight reduction of the power is a consequence of the shock retraction between 100 and 150 ms post bounce. When the composition interface between the Si-layer and the oxygen enriched Si-shell reaches the shock at $\sim$170 ms after bounce and triggers transient shock inflation (cf. Figs. 1, 2, and 5), the power increases again before it decays once more during another period of shock contraction. At $t \gtrsim$ 350 ms a phase of continuous, slow expansion of the shock begins and the low-mode power grows. After 500 ms until the end of our simulation at $\gtrsim$600 ms, the low SASI modes gain another factor of 30 in power (middle panel of Fig. 4), which is accompanied by an accelerating shock expansion. Finally, after 550 ms, the outward motion of the shock speeds up strongly, and Model M15LS-rot enters a runaway situation that most probably initiates an explosion (Figs. 2, 3, and 5). The shock acceleration is supported by the onset of nucleon recombination to α-particles as the hot-bubble medium expands beyond 200 km and cools down to less than $\sim$1 MeV (cf. the light-grey region behind the shock in Fig. 2). The formation of α-particles releases a nuclear binding energy of about 7 MeV per reassembled nucleon and increases the thermal energy of the stellar gas. It thus adds to the energy deposited by neutrino heating and helps bringing the gas in the gain layer to a gravitationally unbound state.

During the outward acceleration at the end of the simulated evolution, the shock in the axisymmetric Model M15LS-rot develops a pronounced butterfly-like shape (bottom right panel of Fig. 3) with a significantly more inflated northern lobe. The nearly unipolar onset of the explosion indicates the dominance of the $l = 1$ SASI mode. The swelling southern and much bigger northern high-entropy plumes of neutrino-heated gas push the shock outward and create a kink in the shock surface near the equator. The kink feature causes accreted gas to hit the shock at an oblique angle and therefore to be deflected at passing the shock. The deflected gas streams from the northern and southern hemispheres collide and

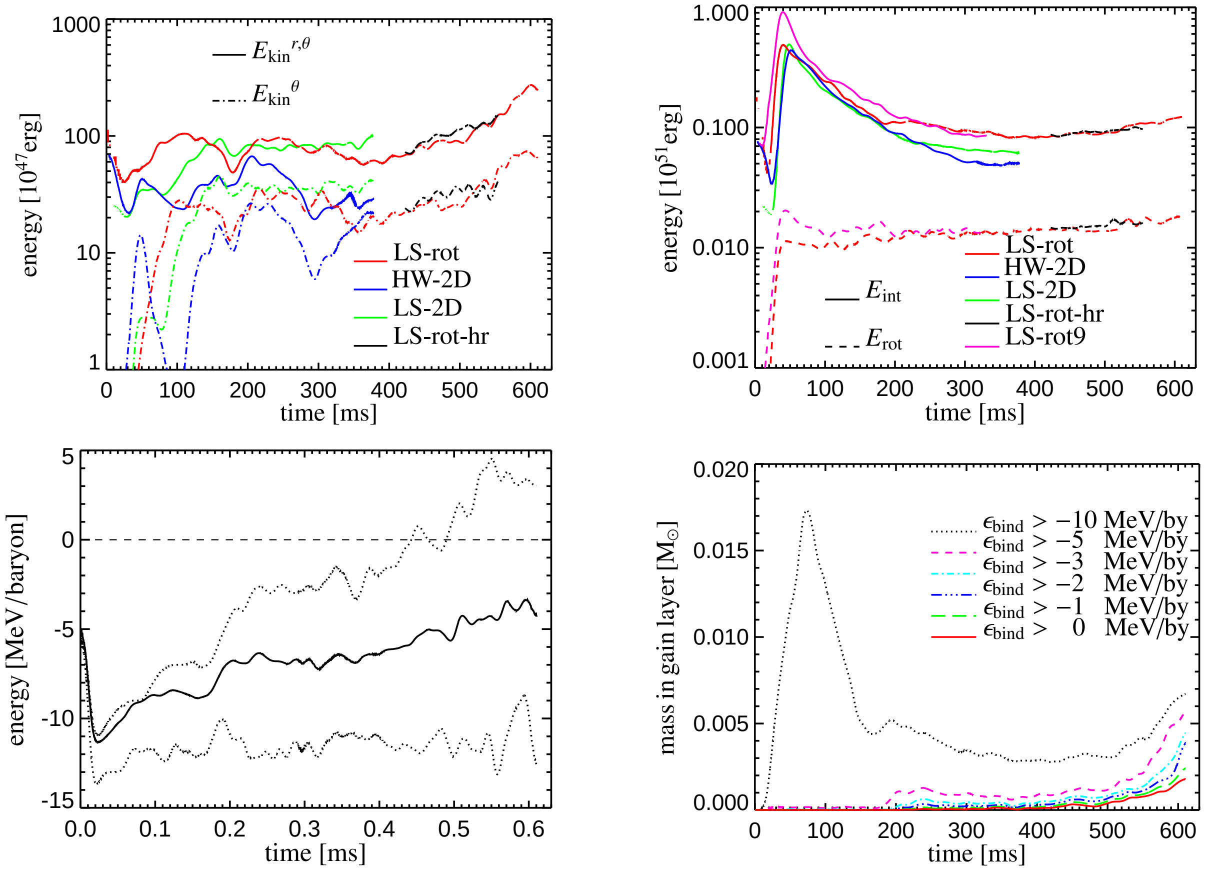

Fig. 8.— The upper plots display integrated energies in the gain layer as functions of post-bounce time for several models of our set of 2D simulations, the lower plots show energies per nucleon and corresponding masses in the gain layer as functions of time for Model M15LS-rot. *Top left*: Kinetic energies $E^{r}_{\rm kin}$ and $E^{r,\theta}_{\rm kin}$ associated with the gas motion in radial and in radial plus lateral direction, respectively. *Top right:* Internal energy and rotational energy. *Bottom left:* Mean total (kinetic, including rotational, plus internal plus gravitational) energy per baryon (thick line) and energy range that contains 90% of the mass in the gain layer of Model M15LS-rot (dotted). *Bottom right:* Masses in the gain layer of Model M15LS-rot with total energies per nucleon above certain values. In the upper two plots, the additional black line between 400 and about 550 ms corresponds to Model M15LS-rot-hr, which is a test calculation of Model M15LS-rot with significantly increased radial resolution in the neutron star surface and neutrino-heating layer.

form a long-lived and waving equatorial downdraft. This accretion funnel collects the major fraction of the equatorially infalling gas and channels it towards the neutron star with supersonic velocities. Gas with low angular momentum, however, collapses closer to the rotation axis and creates very stable polar downflows in both hemispheres. These polar downdrafts are a common feature of all 2D simulations with rotation and their durability and universality can be understood by the Solberg condition, which says that a situation in which the specific angular momentum increases with distance from the rotation axis is stable (see the results and discussion in Scheck et al. 2006).

Rotation, although "modest" in the sense discussed in Sect. 2.2, has an important influence in Model M15LS-rot, but it is not crucial for the evolution after bounce and the final outcome obtained in this simulation. This will be further discussed in Sect. 3.3 by comparing the different models of our set of runs. Until the end of the computation (at ∼610 ms), the neutron star in Model M15LS-rot has contracted to an average radius of 26 km (compared to 21 km for the 1D Model M15LS-1D) with a pole-to-equator radius ratio of 0.65 (eccentricity of 0.76). It rotates strongly differentially with an average period of 3 ms. In the gain layer the rotation period is typically longer than 10 ms.

3.2.2. *Runaway conditions and explosion criteria*

At $t \gtrsim 350$ ms Model M15LS-rot evolves gradually and steadily towards a situation that is more and more favorable for an explosion. This is clearly visible in a number of quantities. Not only the continuous expansion of the shock front (Figs. 2 and 5) but also the mass, energy, and neutrino heating in the gain layer reveal the trend that the explosion conditions become better at later times.

Two timescales are crucial for the behavior of the gain layer: the timescale of accreted matter to be advected from the shock to the gain radius,

$$\tau_{\rm adv} \equiv \frac{R_{\rm s} - R_{\rm g}}{|\,\langle v_r \rangle\,|}\,, \tag{3}$$

and the neutrino heating timescale of the gas in this region,

$$\tau_{\rm heat} \equiv \frac{|E_{\rm bind}|[R_{\rm g},\,R_{\rm s}]}{Q_{\rm heat}} \tag{4}$$

(Janka et al. 2001, Thompson et al. 2005, Buras et al. 2006b). Here $R_{\rm g}$ denotes the average gain radius, $\langle v_r \rangle$ is the average postshock velocity, $E_{\rm bind}$ the total energy of the matter in the gain layer as sum of internal, kinetic, and gravitational energies, and $Q_{\rm heat}$ is the integrated net heating rate by neutrinos. Therefore $\tau_{\rm heat}$ measures the time it takes neutrinos to deposit an energy equal to the binding energy $E_{\rm bind}[R_{\rm gain},\, R_{\rm shock}]$ of the matter in the gain layer, whereas $\tau_{\rm adv}$ can be considered as a measure of the duration the gas is exposed to neutrino energy deposition[3].

Figure 6 shows that along with the growing strength of the low SASI modes (cf. Fig. 4) the advection timescale in Model M15LS-rot rises continuously after 350 ms post bounce, leading to a steady growth of the timescale ratio $\tau_{\rm adv}/\tau_{\rm heat}$ from about 0.6 to values larger that unity. The critical value of unity is exceeded at $\sim$530 ms after bounce and remains larger than unity until the end of the simulation, i.e. for a period of time much longer than the heating timescale $\tau_{\rm heat} \approx 20$ ms. This is a necessary condition for an explosion (see Buras et al. 2006b). Note that even after the shock starts a rapid acceleration at 550 ms, $\tau_{\rm adv}$ can be evaluated because there is net accretion still going on. At the end of our simulation for Model M15LS-rot, about 60% of the matter swept up by the shock is still accreted onto the neutron star, while the rest stays in the gain layer and causes a growth of the mass there at a rate of roughly $0.1\,M_\odot\,{\rm s}^{-1}$ (see the top panel in Fig. 7).

The neutrino-heating timescale of the gain layer in Model M15LS-rot levels off near 20 ms after $t \sim 350$ ms (Fig. 6, middle panel). This corresponds to a rate of neutrino energy deposition of about $4\times 10^{51}\,{\rm erg\,s^{-1}}$ (Fig. 7, middle panel) with a mild increase with time. This increase is a consequence of the slowly growing mass and optical depth of the gain layer and of the higher mean energies of the neutrinos radiated at later times (see Fig. 1 and 9). The corresponding neutrino heating efficiency, defined as ratio of the total net energy deposition to the sum of the radiated ν_e and $\bar\nu_e$ luminosities, rises from about 6% at 350 ms to more than 9% at the end of our simulation.

With the accumulation of mass in the gain layer, also the internal energy in this region grows (Fig. 8, upper right panel). The same is true for the rotation energy of the accreted matter, which rises because the gas that is accreted at later times comes from larger distances and has a higher specific angular momentum. The increase of both energies, however, is rather moderate (some 10%) compared to the growth of the kinetic energy of fluid motions in the gain layer in non-azimuthal directions. Both the energy associated with gas flows in latitudinal direction and with gas motions in radial plus lateral directions gain a factor of roughly four between 350 ms and 610 ms (Fig. 8, upper left plot). This, of course, reflects the increasingly more violent SASI and convective activity in the shocked flow. We note, however, that these energies have values around 10^{49} erg, corresponding to $\sim$0.7 MeV per nucleon, an energy that is dwarfed by the neutrino heating rate (300 MeV s^{-1} per nucleon), applied for a typical timescale $\tau_{\rm adv}$, and the recombination energy of nucleons to α-particles. Accordingly, the total energy per nucleon in the gain layer changes from a mean of about -7 MeV at 350 ms to -3.5 MeV around 600 ms, and a sizable fraction of the mass in the gain layer begins to obtain positive energy towards the end of the computed evolution (Fig. 8, lower two panels).

[3] Note that in multi-dimensional simulations when non-radial hydrodynamic instabilities play an important role, Eq. (3) for evaluating the advection timescale has to be replaced by Eq. (8) of Buras et al. (2006b).

3.2.3. *Role of the SASI*

In the last section we argued that the combination of shock expansion, critical timescale ratio, and growing mass and energy in the gain layer indicates that Model M15LS-rot approaches a runaway situation. The described behavior of these quantities is very similar to the findings of Scheck et al. (2007) for their exploding model W00F (cf. Figs. 19 and 20 in their paper). In the latter model the growth of buoyancy instabilities was initially damped due to the choice of small seed perturbations and a low neutrino-heating rate in the gain layer. In contrast, the larger perturbations that have developed in the stellar core of Model M15LS-rot during the collapse allow convection to begin in this simulation as soon as neutrino heating achieves to create a convectively unstable situation in the gain layer. Therefore the growth of the SASI and of convection cannot be studied separately in the present simulation.

Nevertheless, the large-amplitude low-mode shock oscillations seen in Model M15LS-rot only $\sim$100 ms after bounce (see Fig. 4) clearly indicate the presence of the SASI, whose growth appears to be accelerated by the sonic and vorticity perturbations associated with the convective activity in the postshock region. Systematic studies by Scheck et al. (2007) showed that the SASI can play an important supportive role for neutrino-driven explosions. This was also found in case of an $11.2\,M_\odot$ star, whose evolution until the onset of an explosion (at $\sim$200 ms after bounce) was computed by Buras et al. (2006b). An explosion of this star by the neutrino-heating mechanism could only be obtained when the grid setup allowed for the development of $l = 1$ and $l = 2$ SASI modes. When the lateral grid was constrained to a 90-degree wedge around the equator, in which case the lowest SASI modes were suppressed, the 2D simulations did not yield explosions. In the present $15\,M_\odot$ simulation the SASI seems to play a similarly crucial role as in the $11.2\,M_\odot$ case.

As shown in the studies of Scheck et al. (2007), SASI shock oscillations can develop even in conditions which per se are disfavorable for the growth of convection. Thus the SASI can support the delayed revival of the stalled shock in at least two ways: (i) Large-amplitude SASI expansion and contraction phases of the shock lead to supersonic lateral velocities in the postshock flow and the formation of sheets with very steep unstable entropy gradients. This fosters the development of secondary convection or strengthens the ongoing convective activity. (ii) SASI sloshing motions as well as strong postshock convection do not only produce large non-radial velocity components in the postshock flow but also push the accretion shock to larger radii. This again reduces the average infall velocity in the postshock layer, because the velocity in the free-fall region ahead of the shock drops like $R_{\rm s}^{-1/2}$. A larger shock radius thus leads to a significantly longer advection timescale, roughly $\tau_{\rm adv} \propto R_{\rm s}^{3/2}$.

All these effects help to keep accreted matter in the gain layer for a longer period of time (a consequence of which is the increasing mass in this layer). This supports the energy deposition by neutrinos and thus facilitates the explosion. So, although the kinetic energy associated with the SASI remains negligible for the explosion energetics, once the SASI and convection have pushed the shock sufficiently far out, enhanced neutrino heating and ultimately also the additional energy release by nucleon recombination set up the conditions for runaway.

The contributing effects in the postshock accretion flow, the SASI, convection, and neutrino heating, however, are strongly linked and interdependent in a complex way. In such a highly nonlinear situation it is therefore extremely difficult to exactly determine the influence of each aspect individually. It is, for example, unclear which conditions are primarily responsible for the growth of the SASI power at late post-bounce times (at $t \gtrsim 300\,\mathrm{ms}$), and which role neutrino heating may play in this context. By comparing in Sect. 3.3 Model M15LS-rot with the other simulations of our sample — although it was not yet possible to carry these other runs to equally late times as our reference model — we will strive for a better understanding of the influence of at least some potentially important aspects like rotation and the contraction and growing compactness of the forming neutron star.

3.2.4. *Explosion energy*

At the end of the computed evolution at $t \sim 610\,\mathrm{ms}$ after bounce, Model M15LS-rot has reached runaway conditions that most likely initiate the explosion of the $15\,M_\odot$ star. In order to come up with reliable estimates of the final explosion energy, however, the simulation would have to be continued for many hundreds of milliseconds more. This is obvious from the computations of neutrino-driven explosions performed by Scheck et al. (2007; see Figs. 9 and 10 there) and Scheck et al. (2006; see Appendix C there) and has several reasons. (1) When rapid shock acceleration sets in, only a smaller fraction of the mass in the gain layer starts to attain positive total specific energy (see Fig. 8), and it takes several ten milliseconds until a major part of the mass between shock and gain radius follows the outward motion of the shock and the explosion energy reaches even only some 10^{49} erg (cf. Fig. 10 in Scheck et al. 2007, and Fig. 24 in Buras et al. 2006). (2) Also then the energy of the explosion grows only gradually and initially roughly linearly with a rate of some 10^{50} erg per 100 ms. During this phase ongoing accretion transports fresh gas towards the gain radius, where a part of the gas absorbs energy from neutrinos and begins to rise again, while the rest of the accreted gas is advected into the cooling layer below the gain radius and is added into the forming neutron star. (3) After some time the downdrafts of accreted matter may be quenched and the inflow of gas towards regions near the gain radius may stop, but still more neutrino-heated gas is ejected in the neutrino-driven wind that sheds off matter from the surface layer of the nascent neutron star. During this phase the increase of the explosion energy levels off, but still a significant fraction of the final energy may be added (though with a much lower rate) over timescales of 1–2 more seconds. (4) The total energy injected at the explosion center has to be corrected for the negative total energy of the gravitationally bound outer stellar shells, which are going to be swept out in the blast instead of falling back to the neutron star.

Point (2) implies that simultaneous accretion and outflow of neutrino-heated gas as a generically multi-dimensional phenomenon is an essential feature of the supernova explosion mechanism. The rate at which accreted, cool gas is channelled through the neutrino-heating region, gains energy from neutrinos, and finally rises outward again (the process described in point (2) above) decides about the power that is accumulated in ejected material. Let the corresponding outflow rate of neutrino-heated gas be a fraction ζ of the mass accretion rate $\dot M_{\mathrm{acc}}$ through the shock, i.e., $\dot M_{\mathrm{out}} = \zeta \dot M_{\mathrm{acc}}$. The rate at which energy is pumped into the ejecta can then be estimated very roughly as

$$\begin{aligned}\dot E_{\mathrm{exp}} &\sim \zeta \dot M_{\mathrm{acc}} \dot q_\nu \tau_{\mathrm{adv}} \\ &\sim 2\times10^{51}\,\frac{\mathrm{erg}}{\mathrm{s}}\left(\frac{\zeta}{0.5}\right)\left(\frac{\dot M_{\mathrm{acc}}}{0.2\,M_\odot/\mathrm{s}}\right)\times \\ &\quad\times\left(\frac{\dot q_\nu}{300\,\mathrm{MeV/s}}\right)\left(\frac{\tau_{\mathrm{adv}}}{30\,\mathrm{ms}}\right)\,, \end{aligned}\tag{5}$$

where $\dot q_\nu$ is the average neutrino energy deposition rate per unit of mass in the gain layer, and the advection timescale τ_{adv} through the gain region is a measure of the mean exposure time of the gas to neutrino heating[4]. The numerical values used in Eq. (5) are taken from the conditions at the end of run M15LS-rot (see Figs. 5, 6, 7, and Sect. 3.2.2). We note that the power of the outflow of neutrino-heated matter is seriously underestimated in simulations with Newtonian instead of relativistic gravity, because in the Newtonian case the luminosities and energies radiated by the less compact and cooler neutron star are considerably lower and $\dot q_\nu$ is correspondingly smaller.

With $\dot E_{\mathrm{exp}}$ from Eq. (5) and the duration τ_{acc} of the accretion phase, the explosion energy, in a crude way, can be written as

$$E_{\mathrm{exp}} \approx \dot E_{\mathrm{exp}}\tau_{\mathrm{acc}} + E_{\mathrm{wind}} + E_{\mathrm{burn}} - E_{\mathrm{bind}}\,. \tag{6}$$

Here the first term on the rhs side accounts for the total energy that is transferred by neutrinos to the ejecta during the phase of simultaneous accretion and outflow, the second term measures the integrated power of the neutrino-driven wind that starts after accretion has ceased and matter must be lifted all the way out of the deep gravitational potential at the neutron star surface (the phase mentioned in point (3) above), the third term takes into account additional energy release by nuclear burning in shock-heated matter when the shock wave reaches layers of still unburned nuclear fuel, and the fourth term corrects for the gravitational binding energy of the overlying stellar material (as addressed in point (4) above). For stars around 15–20 $M_\odot$ the last two terms can be estimated to approximately compensate each other (see Janka et al. 2001).

But how long does accretion continue and how long does Eq. (5) therefore apply? The time when accretion ends can be deduced in a crude way from the requirement that at this moment the outgoing shock (with velocity v_{s}

[4] Note that the product $\dot M_{\mathrm{acc}}\tau_{\mathrm{adv}}$ is a fairly accurate measure of the mass in the gain layer at any time after bounce.

and postshock velocity v_2 in the ovserver frame) must accelerate the postshock matter to escape velocity. The corresponding radius is therefore determined by

$$R_{\rm esc} \approx \frac{2\,GM}{v_2^2} \sim 5400\,{\rm km}\; M_{1.5}\, v_{\rm s,9}^{-2}\;, \qquad (7)$$

where $M_{1.5}$ denotes the enclosed mass normalized to $1.5\,M_\odot$, $v_{\rm s,9}$ the shock velocity in $10^9\,{\rm cm\,s^{-1}}$, and the postshock velocity v_2 was determined from the preshock velocity v_1 and the shock velocity $v_{\rm s}$ by the first shock-jump condition as

$$v_2 \;=\; (1-\beta^{-1})v_{\rm s} + \beta^{-1}v_1 \;\approx\; \frac{6}{7}\,v_{\rm s}\;, \qquad (8)$$

with $\beta = \rho_2/\rho_1 \approx 7$ and $v_1 \sim 0$. For the duration of the accretion phase after the onset of outward shock expansion we therefore get:

$$\tau_{\rm acc} \;\approx\; \frac{R_{\rm esc}}{v_{\rm s}} \;\sim\; 0.5\,{\rm s}\; M_{1.5}\, v_{\rm s,9}^{-3}\;. \qquad (9)$$

This means that accretion can easily continue for half a second or even longer, if the shock expands slowly in the beginning. This is confirmed by the supernova simulations of Scheck et al. (2006), in some of which accretion was observed to still go on significantly later than one second after the explosion had started. The explosion energy therefore is not determined by the conditions just at the moment when the outward shock acceleration begins, and it is therefore impossible to conclude from our simulated evolution that the explosion of Model M15LS-rot will finally be weak or strong. In the multi-dimensional environment of the supernova core with accretion and shock expansion being simultaneously present, it is essential to take into account the long-lasting period of mass downflow to the nascent neutron star. Even though the neutrino-driven explosion sets in rather late after bounce in our simulation, Eqs. (5) and (9) suggest that the nonspherical nature of the gas flow in the supernova core, due to which the neutrino-heating region around the neutron star is replenished with fresh gas over a long period of time, may well allow the explosion energy $E_{\rm exp} \sim \dot{E}_{\rm exp}\tau_{\rm acc}$ to reach a canonical value around 10^{51} erg.

3.3. *Comparison of models*

Comparing Model M15LS-rot with the other 2D simulations of our sample allows one to gain insight into various aspects that may have important influence on the post-bounce evolution.

3.3.1. *High-resolution Model M15LS-rot-hr*

Repeating the computation of Model M15LS-rot during the crucial phase of growing SASI power between ∼400 ms and ∼550 ms with finer radial zoning (Model M15LS-rot-hr) does not reveal any resolution deficiencies of our standard run. No important differences are visible in Figs. 5, 6, 7, and 8. It is interesting, however, to note that the transient phase of damped SASI activity in Model M15LS-rot around 500 ms (cf. the middle panel of Fig. 4), which leads to a short pause in the expansion of the average shock radius (Fig. 5) and a step-like interruption of the rise of the advection timescale, is absent in Model M15LS-rot-hr. This suggests that the feature is just a consequence of the chaotic and stochastic behavior of the non-radial hydrodynamic instabilities that stir up the flow between shock front and forming neutron star. The conditions that are favorable for an explosion seem to evolve continuously and a numerical resolution problem in not likely to be the cause of the final runaway in Model M15LS-rot.

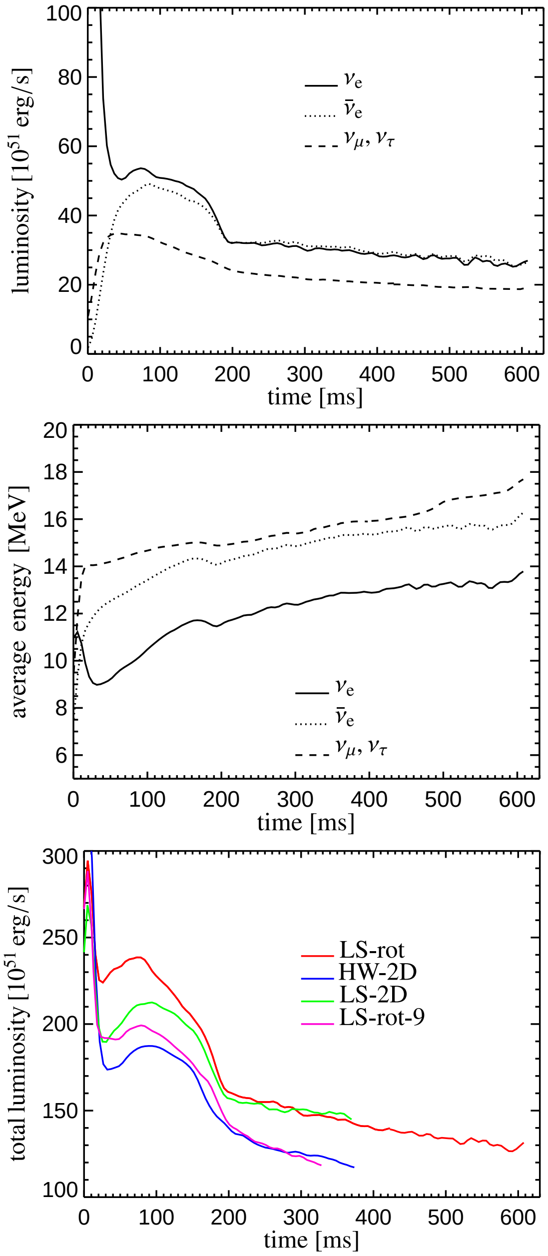

FIG. 9.— Luminosities (*top*) and mean energies (*middle*) of radiated neutrinos in Model M15LS-rot, and total luminosities (summed for neutrinos and antineutrinos of all flavors) for all 2D simulations (*bottom*) as functions of time after bounce. All quantities are evaluated at a radius of 400 km for an observer in the rest frame of the stellar center, and the average energies are defined as ratio of energy flux to number flux.

3.3.2. *Rotating Model M15LS-rot9*

Model M15LS-rot9 was computed with a somewhat weaker effective relativistic gravitational potential than

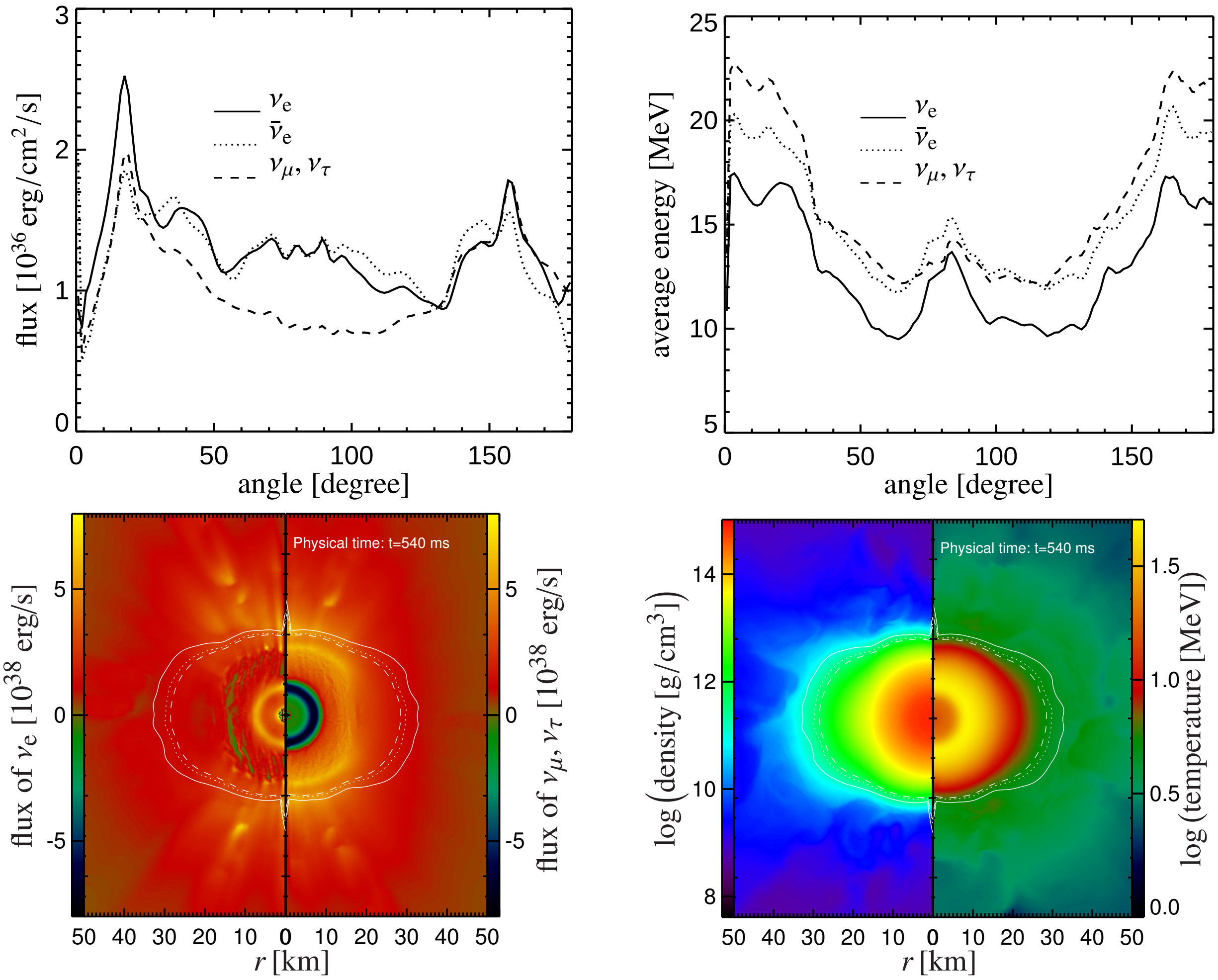

FIG. 10.— *Top:* Neutrino energy fluxes (*left*) and mean energies (*right*) as functions of polar angle at 540 ms after bounce for Model M15LS-rot. The quantities are measured at 400 km and given in the observer frame, and the average energies are defined as ratio of energy flux to number flux. *Bottom, left:* Energy fluxes of electron neutrinos and (one kind of) heavy-lepton neutrinos in and around the nascent neutron star. The mean neutrinospheres, which are marked by white lines for ν_e (solid), $\bar{\nu}_e$ (dotted), and ν_μ (dashed), are significantly deformed because of the presence of rotation. *Bottom, right:* Density and temperature in the vicinity of the forming neutron star.

our standard Model M15LS-rot (Case A of Marek et al. 2006 instead of Case R; the former yields the more accurate treatment for nonrotating stellar core collapse according to comparisons with fully relativistic simulations). A comparison of these two simulations with the nonrotating Model M15LS-2D, which shares the description of the effective relativistic potential with Model M15LS-rot9 (cf. Table 1), allows us to draw conclusions on the importance of rotation and of the strength of the gravitational potential.

Model M15LS-2D without centrifugal effects but with weaker gravity is astonishingly similar to Model M15LS-rot in many of the evaluated aspects. This is true, e.g., for the neutrino luminosities at $t \gtrsim 200$ ms after bounce (bottom panel in Fig. 9) and for the neutrino-heating rate in the gain layer and the heating efficiency (Fig. 7) as well. But also the average shock radii of both models are fairly similar and therefore the advection timescales do not differ much (Figs. 5, 6). The ratio of the advection timescale to the heating timescale shows the same trend in both cases, with a slight time lag of Model M15LS-2D (lower panel of Fig. 6). This suggests that rotation does not play an essential role for the evolution of Model M15LS-rot towards runaway. In fact, with respect to the overall long-time behavior, rotation seems to just compensate much of the influence of the stronger gravitational potential used in Model M15LS-rot.

The weaker gravity in Model M15LS-rot9 relative to Model M15LS-rot allows the shock to move farther out by ~20 km on average during the first 300 ms after bounce (Fig. 5). Since also the infall velocity in the preshock region is lower due to the reduced gravitational acceleration, the advection timescale is significantly longer in Model M15LS-rot9. At the same time, the neutrino luminosities of Model M15LS-rot9, in which the neutron star is less compact and less hot, are somewhat smaller (Fig. 9, bottom panel) and therefore the postshock heating is weaker (Fig. 7) and the heating timescale is considerably longer (Fig. 6) than in Model M15LS-rot. For this reason, Model M15LS-rot9 appears to be less favorable for generating a SASI-aided neutrino-driven explosion than the nonrotating case with the same description of gravity, despite the fact that centrifugal support allows for a larger average shock radius. One might therefore conclude that rotation as considered in our Models M15LS-rot and M15LS-rot9 does *not improve* the conditions for an explosive runaway compared to nonrotating models in which low SASI modes are able to develop (the result, however, turns out to be opposite, if such modes are suppressed by a constraining choice of the grid setup; see Fig. 15 in Buras et al. 2006b).

3.3.3. *Nonrotating Models M15LS-2D and M15HW-2D*

The comparison of Models M15LS-2D and M15HW-2D yields information about the influence of the neutron star EoS, which determines many aspects of the post-bounce evolution, most importantly the compactness of the nascent neutron star and the properties of the radiated neutrinos.

The HW-EoS used in Model M15HW-2D is clearly stiffer and the neutron star consequently less compact (see Figs. 1 and 5). The neutrino luminosities and mean energies are therefore lower (Fig. 1 and the bottom panel of Fig. 9), which leads to a correspondingly reduced heating rate and heating efficiency in the gain layer (Fig. 7), a much longer heating timescale, and thus also to a smaller timescale ratio (Fig. 6).

While in the 1D simulation with the HW-EoS the shock position follows the behavior of the neutron star radius and expands to a larger distance from the center than in the 1D model with the LS-EoS (see Fig. 1 and Eq. (1)), the situation is different for the 2D runs. Here the sloshing shock in Model M15HW-2D reaches a clearly smaller radius than in Model M15LS-2D during most phases of the computed $\sim$ 400 ms of post-bounce evolution. This is particularly obvious between 200 and 300 ms after bounce and points to a significantly lower strength of the SASI activity. An inspection of the kinetic energies in Fig. 8 (upper left panel) supports this conjecture, and a quantitative evaluation reveals that the $l = 1$ and $l = 2$ SASI modes reach only 20–30% of the power they have in Model M15LS-2D. In fact, the SASI activity in Model M15HW-2D grows considerably more slowly and the low-mode power is orders of magnitude smaller than in Model M15LS-2D until nearly 200 ms after bounce.

This suggests that the compactness of the forming neutron star has a very strong influence on the growth and strength of the SASI and of convective activity in the gain layer, either directly by the conversion of gravitational binding energy to kinetic and internal energy in the accretion flow, or indirectly via the effects of larger luminosities and mean energies of the radiated neutrinos and thus stronger neutrino heating. A more rapidly contracting and more compact neutron star is obviously more favorable in this context.

Towards the end of the computed evolution, Model M15HW-2D might begin to reverse its pessimistic trend in comparison with Model M15LS-2D. Quantities like the shock radius (Fig. 5), the kinetic energy in the gain layer (Fig. 8), the SASI power, and the low-mode shock deformation (Fig. 4) exhibit a strong rise after $\sim$300 ms, which leads to an increase of the advection timescale (Fig. 6) and also of the heating in the gain layer (Fig. 7). This improvement could be a consequence of the growing compactness of the nascent neutron star. Both simulations, Model M15HW-2D and Model M15LS-2D, however, could not yet be carried on to a sufficiently late times to see which difference the two employed nuclear EoSs might ultimately make for an explosion at very late times after bounce.

3.4. *Neutrino emission*

In Figs. 9 and 10 we present some results on the neutrino emission of our exploding Model M15LS-rot. In spite of the deeper effective gravitational potential used in this simulation (Case R of Marek et al. 2006), the luminosities and mean energies of the radiated neutrinos at late times after bounce ($t \gtrsim 350$ ms) are slightly lower than those in Model M15LS-1D. This is again the influence of rotation, which compensates some of the consequences of the stronger gravity in Model M15LS-rot, an effect that we have already discussed in the context of comparing Models M15LS-rot and M15LS-2D, whose neutrino luminosities become very similar after 200 ms of post-bounce evolution (see lower panel in Fig. 9).

The mean energies of the neutrinos radiated from Model M15LS-rot (averaged over all observer directions relative to the rotation axis), however, do not exhibit the crossing of $\langle\epsilon_{\bar{\nu}_e}\rangle$ and $\langle\epsilon_{\nu_x}\rangle$ seen in the 1D calculations, although both mean energies get very close (compare the middle panel of Fig. 9 with the lower right panel of Fig. 1). The reason for this difference can be understood from the upper right plot of Fig. 10, which displays the mean energies of radiated neutrinos as functions of polar angle. One can see that in the vicinity of the poles (at latitudes $\theta \lesssim 30°$ and $\theta \gtrsim 160°$) the mean energy of muon and tau neutrinos is clearly higher than that of electron antineutrinos, while away from the poles both are very similar and near the equator their order even reverses. This, as well as the trough-like shape of the curves (which is also visible in the muon and tau neutrino flux, see upper left panel of Fig. 10), is a consequence of the rotational deformation of the neutrinospheric region as visible in the lower two plots of Fig. 10. The superimposed short-wavelength variations of the average radiated energies and of the neutrino fluxes are caused by local downdrafts of accreted matter near the poles and close to the equatorial plane. The neutrino flux production associated with such downdrafts is visible as bright spots above and around the neutrinospheres in the lower left panel of Fig. 10. Near the poles, where the downdrafts penetrate deep inward and become very hot, neutrinos of all flavors are produced in the tips of these flow structures, whereas the lower points of equatorial downflows emit only ν_e and $\bar{\nu}_e$ (this explains the absence of a local maximum of the muon and tau neutrino flux around the equator).

Because of rotation, the density and temperature gradients at the poles (Fig. 10, bottom right) are much steeper and the radial positions of all neutrinospheres there are extremely close together[5]. Most importantly, the region where most of the flux is generated before it gets diluted due to scattering losses and the growing distance from the source, is significantly below the energy-averaged neutrinosphere for muon and tau neutrinos (see the yellow areas in the right half of the lower

[5] In the context of this paper we have adopted Eq. (28) of Buras et al. (2006a) for the definition of the energy-averaged neutrinospheres. This means that the neutrinospheres coincide with the "transport spheres" where neutrinos undergo the transition from diffusion to free streaming, and not with the "energy spheres" where the neutrino production effectively ceases and the neutrinos decouple energetically from the stellar matter.

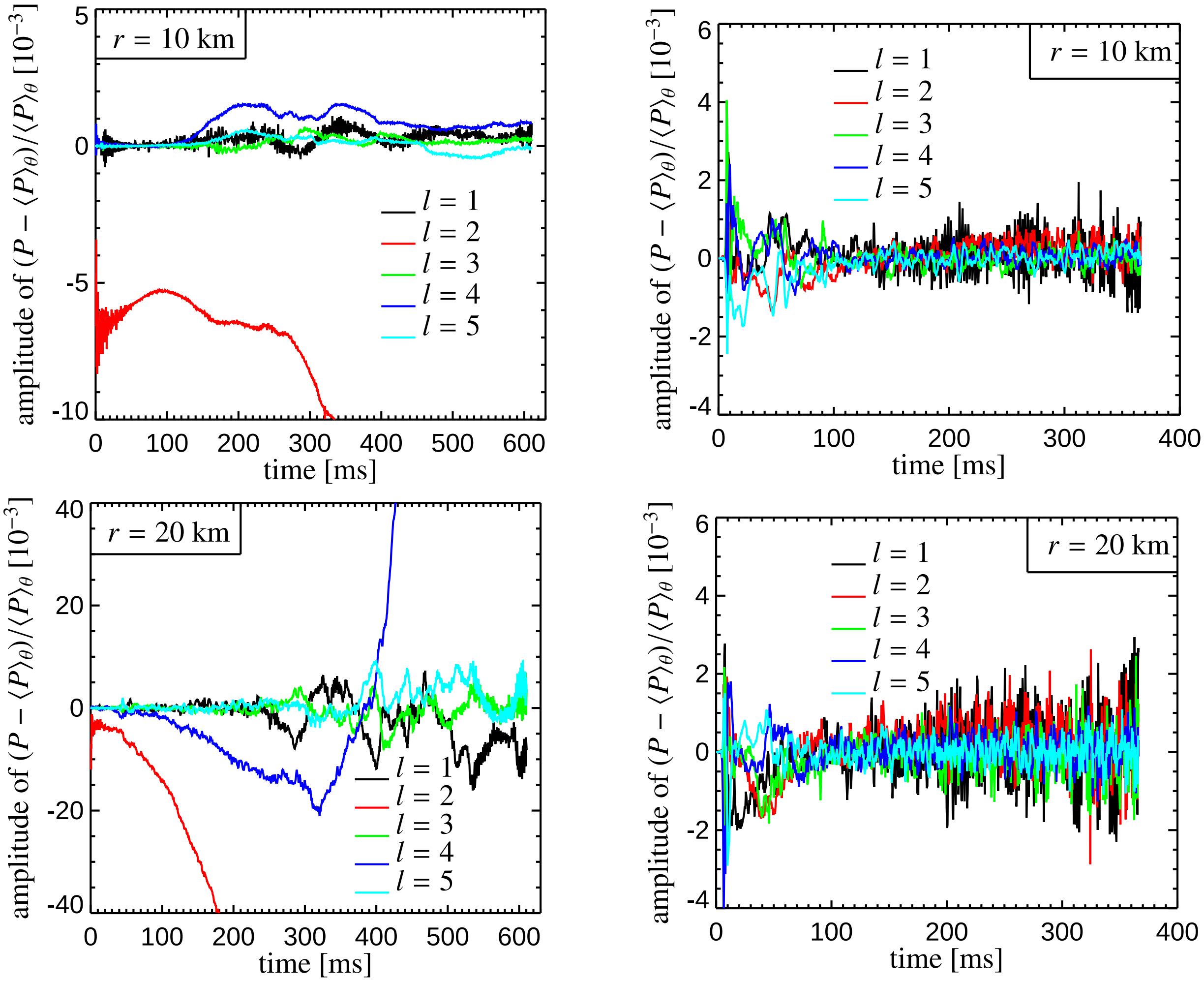

FIG. 11.— Core g-mode oscillations of the nascent neutron star in the rotating 15 $M_\odot$ simulation M15LS-rot (*left*) and in the corresponding nonrotating simulation M15LS-2D (right) as functions of time after bounce. The figures show the amplitudes of the $l = 1$ to $l = 5$ modes of the spherical harmonics expansion of the fractional pressure variations at a radius of 10 km (*top*) and 20 km (*bottom*). Note that the plotted values have to be scaled by a factor 10^{-3} and that the large amplitudes of the $l = 2$ and $l = 4$ terms of Model M15LS-rot reflect the growing influence of rotational asphericity.

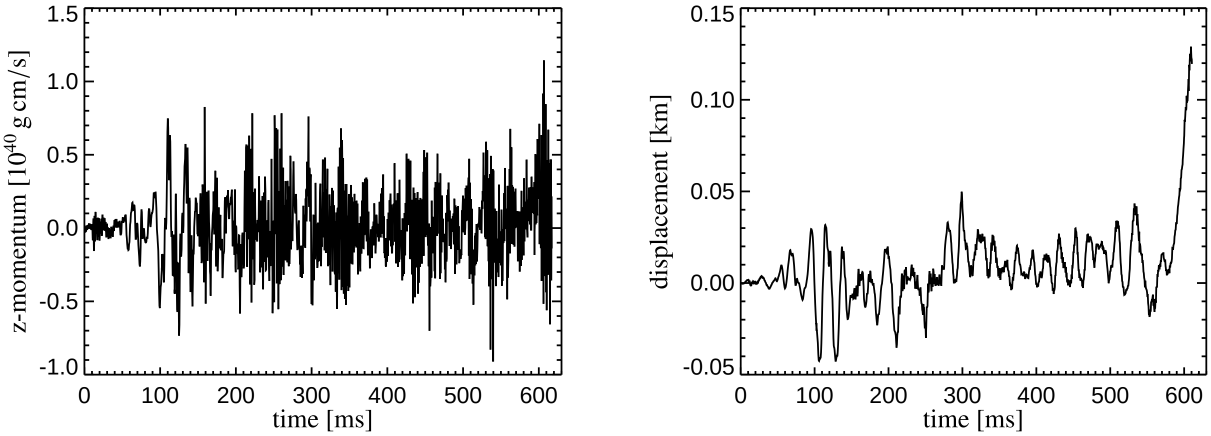

FIG. 12.— Momentum conservation in Model M15LS-rot. The left plot shows the fluctuating total momentum in the direction of the polar (rotation) axis for all gas on the grid, the right plot displays the corresponding displacement of the center of mass from the grid center as function of post-bounce time. During all phases of the computed evolution, this displacement is far less than the radial width of the innermost grid zone (0.3 km).

left plot of Fig. 10). This means that before the ν_μ and ν_τ reach their neutrinosphere, they have to propagate through an extended layer that is inefficient in producing more of these neutrinos, but in which energy transfers in neutrino-nucleon and neutrino-electron scatterings down-grade high-energy neutrinos in energy space. This effect is responsible for the convergence or even inversion of the mean energies of the radiated $\bar{\nu}_e$ and ν_x for a wide range of polar angles, because electron antineutrinos in contrast to heavy-lepton neutrinos are abundantly absorbed and emitted by charged-current β-processes up to their neutrinosphere. Near the poles the extreme steepness of the density gradient and the additional creation of $\nu_\mu\bar{\nu}_\mu$ and $\nu_\tau\bar{\nu}_\tau$ in the accretion downdrafts prevent such a strong "filter effect" of a scattering atmosphere. The 1D models (cf. Sect. 3.1) define a case that is more similar to the equatorial regions of the rotating model: when the mass accretion rate drops strongly after the first $\sim$200 ms of massive post-bounce accretion, the energy sphere of muon and tau neutrinos moves considerably below the neutrinosphere (because the temperature profile becomes steeper), but still the density decline near the neutron star surface is sufficiently gradual to allow for the presence of a layer of frequent neutrino scatterings between the energy sphere and the neutrinosphere of heavy-lepton neutrinos.

Finally, we point out that the region of convective activity inside the nascent neutron star can be discerned in the lower left plot of Fig. 10. In the left half of this figure, which shows the flux of ν_e, a pattern of green and red stripes indicates elongated convective cells that are oriented parallel to the rotation axis. This is typical of a situation in which convection is constrained by the presence of angular momentum gradients (see the discussion in Buras et al. 2006b). The cell structure becomes visible in this image, because Ledoux convection in the newly formed neutron star is driven by negative lepton number gradients and is therefore associated with variations of the neutron-to-proton ratio. Due to the short β-equilibration timescale in the optically thick regime, such variations are tightly linked to differences in the electron neutrino density and flux. In the right half of the lower left image of Fig. 10, one can see that a local maximum of the ν_μ flux coincides with the outer edge of the convective region. This suggests that convection inside the proto-neutron star has a noticeable effect in particular on the transport of muon and tau neutrinos, a fact that was discussed in detail in Buras et al. (2006b).

4. NEUTRON STAR G-MODE OSCILLATIONS

Recently Burrows et al. (2006, 2007b) discovered in their two-dimensional, Newtonian core-collapse simulations that very late after core bounce the newly formed neutron star can be excited to core g-mode oscillations with amplitudes of several kilometers. Burrows et al. did not obtain neutrino-driven explosions in their simulations, but while the shock revealed violent sloshing motions due to the SASI instability, the anisotropic gas flow around the central object remained gravitationally bound and the gas continued to be accreted. After more than one second of post-bounce evolution, however, a rapid outward acceleration of the shock set in. For an $11.2M_\odot$ progenitor, for example, Burrows et al. (2007b) saw this shock revival happening about 1.1 seconds after bounce; in a $20M_\odot$ star the outward shock expansion occurred after 1.2 seconds of post-bounce accretion. In the simulations of Buras et al. (2006b), however, the same $11.2\,M_\odot$ model was found to explode about 200 ms after bounce by the SASI-supported neutrino-heating mechanism. The very late explosions in the runs of Burrows et al. were powered by the acoustic flux that was sent by large-amplitude vibrations of the neutron star into the medium surrounding the compact remnant. On travelling outward, the pressure waves steepened into shocks and dissipated their energy in the medium behind the supernova shock, thus creating the thermal energy that provided the pressure for the shock acceleration.

Burrows et al. (2006, 2007b) estimated that the acoustic energy flux generated by this gravity-wave activity of the forming compact remnant dominates the energy deposition by neutrinos in their models at times later than about one second after bounce. A sizable fraction of the accretion power is thus converted by the oscillating neutron star, which acts as a transducer, to acoustic flux instead of neutrino emission. As long as anisotropic accretion goes on, the gravity waves are further excited and the accretor produces a steady flow of acoustic energy. In order to provide a dynamically relevant rate of energy input to the shock and possibly the supernova explosion, however, the amplitude of the core g-mode oscillations must be sufficiently large at the surface of the nascent remnant; several kilometers seem to be necessary for creating an acoustic energy flux of a few $10^{50}\,\mathrm{erg\,s^{-1}}$ (Burrows et al. 2007c).

Does acoustic power radiated by the newly formed neutron star contribute to the shock revival in our simulations at any significant level? Are core g-mode oscillations excited to relevant amplitudes in our models? In order to answer these questions, we have performed a mode analysis of the gravity-wave activity in the region below the neutrinosphere. Guided by Fig. 7 of Burrows et al. (2006), we show the $l = 1, ..., 5$ amplitudes of the spherical harmonics expansion of the fractional pressure variations $[P(r,\theta) - \langle P(r,\theta)\rangle_\theta]/\langle P(r,\theta)\rangle_\theta$ at $r = 10$ km und $r = 20$ km as functions of time for Model M15LS-rot and the corresponding nonrotating Model M15LS-2D in Fig. 11.

All amplitudes of the core g-modes in our models — except those of the $l = 2$ and $l = 4$ terms in Model M15LS-rot, which reflect the growing rotational deformation of the neutron star in this case — are in the same range of values and roughly two orders of magnitude smaller than the amplitudes seen by Burrows et al. (2006) at the time when their models are going to explode. The acoustic energy flux radiated by the ringing neutron star in our simulations is therefore negligible compared to neutrino heating behind the shock, which typically deposits energy at a net rate of 3–4$\times10^{51}$ erg/s at $t > 200$ ms after bounce. Until the explosion in Model M15LS-rot is initiated by neutrino heating at about 600 ms, there is no sign of any significant energy transfer to the shock by pressure waves that originate from the neutron star. Our models (the $11.2\,M_\odot$ progenitor investigated by Buras et al. (2006b) as well as the $15\,M_\odot$ star considered here) develop neutrino-driven explosions long before the acoustic mechanism was found to cause an explosion in the simulations of Burrows et al. (2006, 2007).

But is our code able to follow core g-mode oscillations,

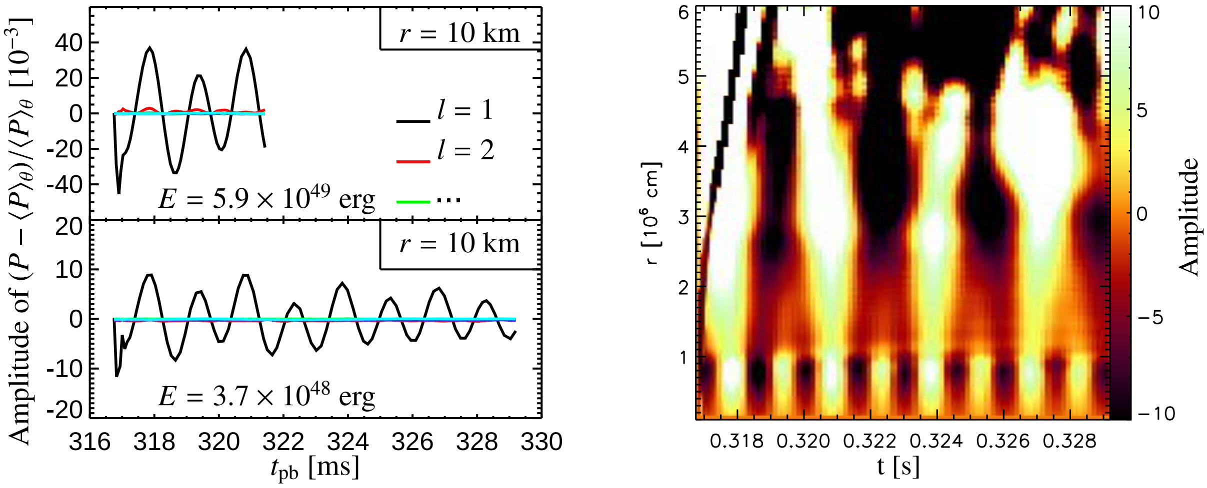

FIG. 13.— *Left:* Test simulations with artificially excited core g-mode oscillations of dipole ($l = 1$) character in the neutron star (here in case of Model M15HW-2D). Two different amplitudes of the initially imposed velocity field were used, 5×10^7 cm/s and 2×10^8 cm/s, corresponding to a factor of 16 different kinetic energies (as indicated in the plot). The clear presence of many cycles of the dipole oscillation demonstrates the ability of our numerical code to follow such gravity waves, if they are instigated. *Right:* The amplitude of the $l = 1$ mode shown in the lower panel of the left plot is displayed here as function of time and radius (a scaling factor of 10^{-3} should be applied for the plotted values). Interior to about 10 km the core oscillates with twice the frequency of the mantle outside of $r \approx 25$ km. In the intermediate, convective layer the gravity waves are damped and the frequency shift happens. At radii $r \gtrsim 50$ km one can see the influence of gravity waves produced by the violent convective overturn and SASI activity in the layer beween gain radius and shock.

in particular of $l = 1$ type, in which case the gas in the stellar center participates in the motion? Since a few radial zones in the central $\sim$1.5 km of our numerical grid are treated in spherical symmetry (to get around too restricted CFL timesteps), one might wonder whether a flow pattern with gas motion through the stellar center can be reasonably well described. Such a spherical core might create severe perturbations, for example because the central mass, which cannot move out of the grid center, absorbs linear momentum and thus causes a significant violation of momentum conservation. In Fig. 12, left plot, the evolution of the total linear momentum of the whole gas on the computational grid (about 2 $M_\odot$, of which about three quarters are contained by the neutron star) is shown for Model M15LS-rot. The right plot of this figure displays the corresponding displacement that the gas mass experiences in the direction of the polar grid axis (which coincides with the rotation and symmetry axis of the 2D model). Due to the rapidly varying g-mode amplitudes (compare Fig. 11), the sign of the linear momentum changes on timescales of only milliseconds (typical g-mode frequencies are 100–500 Hz). The net displacement therefore remains very small: the gas mass wobbles around the grid center with an amplitude of usually less than 50 meters, which is much smaller than the radius of our innermost grid cell (300 meters). Only after the outward shock acceleration has set in, the center of mass and the grid center become separated by about 130 meters. The displacement as a function of time actually reflects mainly the quasi-periodic SASI sloshing motions of the gas mass between shock and neutron star, which have typical frequencies around 50–70 Hz (see Fig. 4), while the tiny core g-mode oscillations cause only a superimposed, high-frequency modulation with a much lower amplitude of the net displacement.

Another potential restriction of our simulations might be connected to our use of a relativistic monopole potential, whose dominant contribution to the gravitational potential of the neutron star prohibits to accurately account for the response of the gravitational field to the nonradial asymmetry of the mass distribution caused by the core g-mode oscillations. One should note here, however, that we still have included the higher multipoles of the gravitational potential in the Newtonian description, and thus our treatment of the gravitational effects is certainly much less constraining and much less approximative than the so-called Cowling approximation, which is widely used for discussing stellar pulsations in the linear regime, although it ignores the influence of the oscillation-induced density variations on the gravitational field.

In order to test whether our code can handle $l = 1$ core g-modes with large amplitudes if they were excited (e.g. hydrodynamically by anisotropic accretion), we artificially instigated a large dipole g-mode by imposing an $l = 1$, $n = 1$ (i.e., we assumed one radial node) perturbation of the z-component of the velocity field at a time late after bounce. The imposed velocity field was chosen such that the linear momentum associated with the perturbation was zero, and the once perturbed model was followed in its evolution with all (micro)physics being the same as in the long-time supernova runs. For exploring the response to g-modes with different energies, we varied the amplitude of the imposed velocity perturbation. Figure 13 displays results of two such tests in case of Model M15HW-2D. One can see that after an initial, short relaxation (caused by the fact that our chosen velocity perturbation did not correspond to an eigenfunction) an essentially pure dipole mode develops with a clean periodicity of the fractional pressure variations at a given radius. The amplitudes of these variations are factors of about 5 and 20 larger than those which we find for the core g-modes in our supernova runs (see Fig. 11).

The test model with the low g-mode energy was run for many cycles and shows a decrease of the oscillation amplitude by approximately a factor of two on a timescale of about 15 ms. This decay is mainly caused by the acoustic flux that sends energy from the neutron star surface into the surrounding medium. Since roughly 75% of the initial mode energy are lost within 15 ms, we estimate an acoustic energy flux of nearly $2 \times 10^{50}\,\mathrm{erg\,s^{-1}}$, comparable to the value stated by Burrows et al. (2007c). In our supernova runs without artificial g-mode excitation and thus five times smaller g-mode amplitudes, the energy flux from the oscillating neutron star should be roughly 25 times lower and therefore minuscule compared to neutrino energy deposition behind the shock. The test calculation with the larger excitation amplitude was computationally expensive and was therefore continued only for about two full oscillation cycles, because the g-mode induced variations of the thermodynamic quantities led to shifts of the β-equilibrium between neutrinos and the stellar gas. The resulting large neutrino source terms enforced small timesteps in the neutrino transport.

These tests support our confidence that our long-time simulations should be able to trace also large-amplitude core g-modes, if any mechanism existed that drives their excitation. We have no reason to suspect that our numerical code and calculations might fail to handle the hydrodynamic mechanism that Burrows et al. (2006, 2007) considered as responsible for instigating the large core g-modes in their models. Therefore we conclude that the conditions for such an efficient excitation of core g-modes are not present in the central regions of our simulated supernovae.

5. DISCUSSION AND CONCLUSIONS

We have presented evidence from our 2D neutrino-hydrodynamic stellar core-collapse simulations that the neutrino-driven mechanism may explain the explosions of progenitor stars in a wider range of masses. In this work we considered a $15\,M_\odot$ model (s15s7b2 of Woosley & Weaver 1995), which is a typical representative of supernova progenitors in the intermediate mass range between somewhat more than $10\,M_\odot$ and around $20\,M_\odot$. Similar to the explosion obtained for an $11.2\,M_\odot$ star by Buras et al. (2006b), the delayed shock revival by neutrino heating in the $15\,M_\odot$ model was fostered and enabled by the presence of a strong, low-mode SASI oscillation of the postshock layer. The SASI modes develop rapidly in the accretion flow to the neutron star even when convection in the gain layer is initially weak because the growth of this buoyancy instability is damped in the rapidly infalling gas behind the accretion shock.

The SASI has two crucial consequences, which are favorable for the possibility of neutrino-driven explosions. On the one hand, the violent sloshing motions of the postshock layer with fast expansion and contraction phases of the shock create steep entropy gradients in the postshock flow, which lead to powerful secondary convection and thus efficient overturn of the gas in the gain region (for a detailed discussion, see Scheck et al. (2007). On the other hand, the SASI also pushes the shock to larger average radius. This reduces the mean accretion velocity in the gain layer (because the velocity in the infall region ahead of the shock drops inversely with the square root of the shock radius) and thus increases the advection timescale of gas from the shock to the gain radius. The accreted matter is therefore exposed to neutrino heating for a longer time, a fact that is reflected by a significant increase of the critical ratio of the advection timescale to the neutrino-heating timescale. A strong SASI activity has the consequence that this timescale ratio comes much closer to the value of unity, signaling favorable conditions for a neutrino-driven explosion. The combination of these effects indeed turned out to drive the $15\,M_\odot$ model towards a runaway instability at about 600 ms after core bounce (while for the $11.2\,M_\odot$ star this happened roughly 200 ms after bounce, see Buras et al. 2006b).

The energy of such SASI-supported, neutrino-driven explosions, however, is not determined at the moment when the runaway sets in. Instead, accretion of gas towards the gain radius and the neutron star can proceed at the same time as shock acceleration sets in due to the expansion of rising, neutrino-heated, buoyant gas. This characterizes the generically multi-dimensional nature of the developing explosion. The ongoing accretion continuously channels fresh material, which is swept up by the shock, to the region near the gain radius, where neutrino heating is strongest. Roughly half of the gas penetrates to the cooling layer below the gain radius and ultimately settles onto the neutron star, the other half absorbs with high efficiency energy from the neutrinos radiated by the neutron star. This gas turns around and rises again, driven by buoyancy forces, and contributes to the energy of the explosion. Our estimates show (and hydrodynamic simulations by Scheck et al. 2007 have demonstated) that simultaneous accretion and shock acceleration can go on for many hundred milliseconds and therefore the final explosion energy can only be determined by computations that cover a much longer evolution time than we were able to follow in our current simulations. Our analytic considerations, based on the situation at the onset of the explosion, reveal that a canonical value of 10^{51} erg for the explosion energy is well in reach of the considered $15\,M_\odot$ star. The final explosion energy increases sensitively when the initial expansion of the shock is not too fast and when the progenitor maintains an appreciable mass accretion rate for a longer time.

The strong shock acceleration, which we found to begin about 600 ms after bounce in the investigated $15\,M_\odot$ model, is associated with a large dipolar deformation of the shock. This is a clear indication for the dominance of the lowest nonradial SASI mode at the onset of the runaway. It suggests that the developing explosion is likely to be very asymmetric, similar to the artificially initiated neutrino-driven explosions that were computed by Scheck et al. (2006) and led to neutron star kick velocities (with maximum values of more than $1000\,\mathrm{km\,s^{-1}}$) in agreement with measurements. Also the large-scale anisotropies and mixing processes that can be found in many supernova explosions and that seem to determine the appearance of the gaseous supernova remnants might be explained by the large asymmetry of the developing explosion in our $15\,M_\odot$ simulation (see Kifonidis et al. (2006) for studies of the long-time evolution of anisotropic neutrino-driven explosions).

We compared 2D simulations with and without rotation and with a stiff and a soft nuclear equation of state, the former leading to a more rapidly contracting and more compact nascent neutron star. Moreover, we tested the influence of different prescriptions of the effective relativistic gravitational potential in our approximation to relativistic simulations. We found that a faster neutron star contraction (and similarly a stronger gravitational potential) have a favorable influence for the SASI-supported neutrino-driven mechanism. This is caused on the one hand by a more rapid growth of low SASI modes, amplified by the release of gravitational binding energy, and on the other hand by higher luminosities and mean energies of the emitted neutrinos and thus stronger neutrino heating in the gain layer. The latter also has a helpful influence on the development of strong SASI and convective activity in the postshock layer. Rotation, in contrast, can be diagnosed to have the opposite effect. Although centrifugal support leads to a larger average shock radius, a longer advection timescale of the matter falling through the gain layer, and a reduced binding energy of accreted matter, these helpful effects are more than compensated by lower luminosities and mean energies of the neutrinos radiated by the significantly more extended and cooler rotating proto-neutron star. The neutrino heating found in rotating models is considerably lower and the neutrino heating timescale in the gain layer correspondingly longer. The critical ratio of advection timescale to heating timescale therefore signals less favorable conditions for an explosion in comparison with a nonrotating model with otherwise the same physics.

We cannot detect any important influence of core g-mode oscillations in our simulations. The amplitudes of gravity-mode oscillations in the neutron star core remain roughly a factor of hundred lower in our models than in the supernova calculations of Burrows et al. (2006, 2007) at the time they see acoustically driven explosions developing. Our models explode significantly earlier by the neutrino-driven mechanism and the input of acoustic power by the g-modes in the nascent neutron star is minuscule compared to neutrino heating.

Certainly, our current simulations can only be suggestive for how neutrino heating and hydrodynamic instabilities in collapsing stellar cores may conspire to initiate the supernova explosion. Although the positive trend towards a SASI-supported, neutrino-driven runaway late after bounce seems to be a robust feature of our simulations with the softer Lattimer & Swesty (1991) EoS, the exact moment of the onset of the explosion may depend on various uncertain aspects like the amount of rotation in the stellar core, the possible influence of amplifying magnetic fields, unsettled details of the equation of state and of neutrino-matter interactions, the missing treatment of lateral neutrino fluxes in our simulations, and the approximative description of the effects of relativistic gravity. Simulations in full relativity are certainly desirable, in particular for stellar core collapse with rotation, because in this case the optimal choice of the effective gravitational potential is not obvious (see Marek et al. 2006). Systematic long-time simulations for different nuclear equations of state are needed to explore the differences at times later than covered by our present calculations. Moreover, supernova modeling in three spatial dimensions must be the ultimate goal, because the growth rate and properties of the hydrodynamic instabilities in 3D are likely to differ from the axially symmetric 2D case, and new degrees of freedom may play a non-negligible and potentially helpful role, for example spiral waves and triaxial instabilities (see, e.g., Blondin & Mezzacappa 2007, Ott et al. 2007).

In the light of our present results, supernova explosions appear to be an *accretion instability* rather than an aspherical wind as described by Burrows et al. (2007c). The SASI and convective instabilities, and in particular the simultaneous presence of accretion and outflow of neutrino-heated gas, which drives the shock expansion, are crucial ingredients of the explosions described in this paper and constitute the explosions as a generically multi-dimensional phenomenon. The gas outflow during the main phase of shock revival and the build-up of the explosion energy is fed by neutrino-heated, accreted gas. Only much later, after the accretion has ceased, does the gain radius retreat to the neutron star surface and the cooling layer between neutrinosphere and gain radius shrinks to a very narrow region or disappears completely. This marks the onset of the neutrino-driven baryonic wind phase, in which the dilute gas outflow from the nascent neutron star is determined solely by the conditions at the surface of the hot, compact remnant and not by the (accretion) properties of the dying star.

We are very grateful to R. Buras, K. Kifonidis, B. Müller, E. Müller, and M. Rampp for their input to various aspects of the reported project, to R. Johanni for his support in parallelizing our code, and to S. Woosley for data of his progenitor model. This work was supported by the Deutsche Forschungsgemeinschaft through the Transregional Collaborative Research Centers SFB/TR 27 "Neutrinos and Beyond" and SFB/TR 7 "Gravitational Wave Astronomy", the Collaborative Research Center SFB-375 "Astro-Particle Physics", and the Cluster of Excellence "Origin and Structure of the Universe" (`http://www.universe-cluster.de`). The computations were performed on the IBM p690 of the John von Neumann Institute for Computing (NIC) in Jülich, on the national supercomputer NEC SX-8 at the High Performance Computing Center Stuttgart (HLRS) under grant number SuperN/12758, on the IBM p690 of the Computer Center Garching (RZG), and on the sgi Altix 3700 of the MPI for Astrophysics.

REFERENCES

Bethe, H.A. & Wilson, J.R. 1985, ApJ, 295, 14
Blondin, J.M. & Mezzacappa, A. 2007, Nature, 445, 58
Blondin, J. M., Mezzacappa, A., & DeMarino, C. 2003, ApJ, 584, 971
Bruenn, S. W. & Dineva, T. 1996, ApJ, 458, L71
Buras, R., Rampp, M., Janka, H.-T., & Kifonidis, K. 2003a, Phys. Rev. Lett., 90, 241101
Buras, R., Janka, H.-Th., Keil, M.Th., Raffelt, G., & Rampp, M. 2003b, ApJ, 587, 320
Buras, R., Rampp, M., Janka, H.-T., & Kifonidis, K. 2006a, A&A, 447, 1049
Buras, R., Janka, H.-T., Rampp, M., & Kifonidis, K. 2006b, A&A, 457, 281
Burrows, A., Hayes, J., & Fryxell, B.A. 1995, ApJ, 450, 830
Burrows, A., Livne, E., Dessart, L., Ott, C.D., & Murphy, J. 2006, ApJ, 640, 878
Burrows, A., Dessart, L., Livne, E., Ott, C.D., & Murphy, J. 2007a, ApJ, 664, 416

Burrows, A., Livne, E., Dessart, L., Ott, C.D., & Murphy, J. 2007b, ApJ, 655, 416
Burrows, A., Dessart, L., Ott, C.D., & Livne, E. 2007c, Phys. Rep., 442, 23
Colgate, S.A. & White, R.H. 1966, ApJ, 143, 626
Dessart, L., Burrows, A., Livne, E., & Ott, C.D. 2006, ApJ, 645, 534
Foglizzo, T., Scheck, L., & Janka H.-Th. 2006, ApJ, 652, 1436
Fryer, C.L. 1999, ApJ, 522, 413
Fryer, C.L. & Warren, M.S. 2002, ApJ, 574, L65
Fryer, C.L. & Warren, M.S. 2004, ApJ, 601, 391
Heger, A., Woosley, S.E., & Spruit H.C. 2005, ApJ, 626, 350
Herant, M., Benz, W., Hix, W.R., Fryer, C.L., & Colgate, S.A. 1994, ApJ, 435, 339
Hillebrandt, W. 1994, in Supernovae, ed. S.A. Bludman, R. Mochkovitch, & J. Zinn-Justin (Amsterdam: North-Holland), 251
Hillebrandt, W. & Wolff, R.G. 1985, in Nucleosynthesis: Challenges and New Developments, ed. W.D. Arnett & J.W. Truran (Chicago: Univ. Chicago Press), 131
Hillebrandt, W., Wolff, R.G., & Nomoto, K. 1984, A&A133, 175
Janka, H.-T. 2001, A&A, 368, 527
Janka, H.-T. & Müller, E. 1996, A&A, 306, 167
Janka, H.-T., Kifonidis, K., & Rampp, M. 2001, in Physics of Neutron Star Interiors, ed. D. Blaschke, N.K. Glendenning, & A. Sedrakian, Notes in Physics, Vol. 578 (Berlin: Springer), 333; astro-ph/0103015
Janka, H.-T., Marek, M., & Kitaura, F.-S. 2007a, in Supernova 1987A: 20 Years After: Supernovae and Gamma-Ray Bursters, ed. S. Immler, K.W. Weiler, & R. McCray (New York: AIP), in press; arXiv:0706.3056
Janka, H.-Th., Langanke, K., Marek, A., Martínez-Pinedo, G., & Müller B. 2007b, Phys. Rep., 442, 38
Keil, M.Th., Raffelt, G., & Janka, H.-Th. 2003, ApJ, 590, 971
Kifonidis, K., Plewa, T., Scheck, L., Janka, H.-Th., & Müller,E. 2006, A&A, 453, 661
Kitaura, F. S., Janka, H.-T., & Hillebrandt, W. 2006, A&A, 450, 345
Köhler, H.S. 1975, Nucl. Phys. A258, 301
Langanke, K., Martínez-Pinedo, G., Sampaio, J.M., Dean, D.J., Hix, W.R., Messer, O.E.B., Mezzacappa, A., Liebendörfer, M., Janka, H.-Th., & Rampp, M. 2003, Phys. Rev. Lett., 90, 241102
Lattimer, J.M. & Swesty, F.D. 1991, Nucl. Phys. A535, 331
Lattimer, J.M. & Prakash, M. 2007, Phys. Rep., 442, 109
Lattimer, J.M., Pethick, C.J., Ravenhall, D.G., & Lamb, D.Q. 1985, Nucl. Phys., A432, 646
Liebendörfer, M., Rampp, M., Janka, H.-Th., & Mezzacappa, A. 2005, ApJ, 620, 840
Marek, A. 2007, PhD Thesis, TU München
Marek, A., Janka, H.-Th., Buras, R., Liebendörfer, M., & Rampp, M. 2005, A&A, 443, 201
Marek, A., Dimmelmeier, H., Janka, H.-Th., Müller, E., & Buras, R. 2006, A&A, 445, 273
Mayle, R. & Wilson, J.R. 1988, ApJ, 334, 909
Müller, E. & Steinmetz, M. 1995, Computer Phys. Commun., 89, 45
Müller, E., Rampp, M., Buras, R., Janka, H.-Th., & Shoemaker, D.H. 2004, ApJ, 603, 221
Nomoto, K. 1984, ApJ, 277, 791
Nomoto, K. 1987, ApJ, 322, 206
Ott, C.D., Dimmelmeier, H., Marek, A., Janka, H.-Th., Hawke, I., Zink, B., & Schnetter, E. 2007, Phys. Rev. Lett., 98, 261101
Raffelt, G.G. 2001, ApJ, 561, 890
Rampp, M., Janka, H.-Th. 2002, A&A, 396, 361
Scheck, L., Kifonidis, K., Janka, H.-Th., & Müller, E. 2006, A&A, 457, 963
Scheck, L., Janka, H.-Th., Foglizzo, T., & Kifonidis, K. 2007, A&A, submitted; arXiv:0704.3001
Shen, H., Toki, H., Oyamatsu, K., & and Sumiyoshi K. 1998, Nucl. Phys. A637, 435
Thompson, T. A., Quataert, E., & Burrows, A. 2005, ApJ, 620, 861
Wilson, J.R. 1985, in Numerical Astrophysics, ed. J.M. Centrella, J.M. LeBlanc, & R.L. Bowers (Boston: Jones and Bartlett Publ.), 422
Wilson, J.R. & Mayle, R. 1988, Phys. Rep., 163, 63
Wilson, J.R. & Mayle, R. 1993, Phys. Rep., 227, 97
Woosley, S. E. & Weaver, T. A. 1995, ApJS, 101, 181
Woosley, S. E., Heger, A., & Weaver, T. A. 2002, Reviews of Modern Physics, 74, 1015
Yamasaki, T. & Yamada, S. 2007, ApJ, 656, 1019